UNIVERSITY OF NAIROBI

SCHOOL OF PHYSICAL SCIENCES

STRUCTURAL AND ELECTRONIC STUDIES OF SELECTED TITANIUM OXIDES AND OXYNITRIDES

By

LYNET ALLAN

REG.NO: I56/12156/2018

A Thesis Submitted in Partial Fulfilment of the Requirements for the Degree of Master of Science in Physics at the University of Nairobi

June, 2021

DECLARATION

I declare that this thesis is my own work and has not been submitted elsewhere for examination. Where other people's work has been used, this has appropriately been acknowledged and referenced in compliance with the University of Nairobi's regulations.

Signature:................................... Date:......June 30,2021...................

Lynet Allan

I56/12156/2018.

Department of Physics

School of Physical Sciences, University of Nairobi

This thesis is submitted with our approval as the University supervisors.

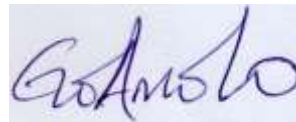|	**Signature**	**Date**
Prof. Julius M. Mwabora,		2nd July 2021
Department of Physics,		
The University of Nairobi.		
Prof. George Amolo,		1st July, 2021
School of Physics and Earth Sciences,		
The Technical University of Kenya.		
Dr. Silas Mureramanzi,		June 30, 2021
Department of Physics,		
The University of Nairobi.		

ABSTRACT

Titanium dioxide (TiO_2) is an abundant, chemically stable, non-toxic, and highly versatile material, with applications ranging from photovoltaics to catalysis. TiO_2 rutile and anatase have band gaps of 3.0 eV and 3.2 eV, respectively, which is too large to absorb visible light, resulting in low photocatalytic efficiency. Efforts have been undertaken to generate a band gap suited for solar energy absorption in order to improve TiO_2's photo-activity under visible light (400 nm to 700 nm). Nitrogen doping into TiO_2 in particular has been able to narrow its band gap, resulting in an absorption tail in the visible-light region. However, TiO_2 has limits to which it can be doped suggesting investigations of the oxygen-deficient corundum Ti_2O_3. Using the state-of-the-art density functional theory (DFT), in the Quantum ESPRESSO package, the properties of the oxides were studied and presented in this work. The structural and electrical properties of the oxides were computed using the generalized gradient approximation (GGA). Ti_2O_3 exhibited metallic properties, yet it has been reported to have semi-conducting characteristics experimentally leading an improved prediction of the bandgaps of the oxides using the DFT+U approach. On doping, the band gaps of N doped TiO_2 structures were reduced as dopant concentration was increased. Mid gap states, having shallower energies in 4%N doping than 2%N cases, were observed in N: TiO_2 structures. However, $Ti_nN_2O_{2n-3}$, n=2, appeared to have a higher absorption threshold than other Ti-based oxides such as TiO_2, N: TiO_2, and Ti_2O_3. The most stable sample of the oxynitrides ($Ti_2N_2O\_P1$) had a gap of 2.2 eV, this is clearly near the middle of visible light and did not have mid-gap states. This suggests that they are more efficient visible-light-driven materials for photocatalytic applications compared to TiO_2, N: TiO_2, and Ti_2O_3.

ACKNOWLEDGMENTS

First and foremost, I acknowledge that the Almighty God has orchestrated my studies, placing in my path certain remarkable persons and opportunities that have served as pillars in the pursuit and completion of my studies.

I am profoundly grateful to my supervisors, Prof. Julius Mwabora, Prof. George Amolo and Dr. Silas Mureramanzi for their close attention, vigilance, and encouragement during this research. Prof. Amolo not only introduced me to computational physics, but led me through it with great skill, comprehension, and motivation.

I am grateful to the International Science Program (ISP), which supported my studies through the condensed matter thematic group of the Department of Physics, University of Nairobi. The Centre for High-Performance Computing (CHPC), Republic of South Africa, through the project MATS862, is recognized for providing access to the HPC cluster facility used in this research.

Many thanks to Perpetua Muchiri, Dr. Michael Atambo, and the entire materials modeling team at the Technical University of Kenya who took time out of their schedules to provide suggestions that made this work possible.

Finally, I owe a great appreciation to my husband, Dr. Moses Ochola, and our babies, who have been gracious enough to allow me to be away while making significant sacrifices to deal with my absence and providing all humanly possible assistance. I will be forever grateful and indebted to you.

DEDICATION

To God be the glory, great things He has done.

TABLE OF CONTENTS

LIST OF TABLES

LIST OF FIGURES

LIST OF SYMBOLS AND ABBREVIATIONS

In this thesis, the symbols and acronyms listed below have been used.

a and c	Lattice parameters /cell dimensions
B3LYP	Becke, Lee-Yang-Parr
BZ	Brillouin Zone
CB	Conduction Band
CBM	Conduction Band Minimum
DFT	Density Functional Theory
DFT+U	Density Functional Theory with Coulomb interaction
DOS	Density of states
E_{cut}	Cut-off kinetic energy
ecut'rho'	Cut –off charge density
E_{tot}	Total Energy
GGA	Generalized Gradient Approximation
GW	Green's function and dynamically screened coulomb interactions
H	Hamiltonian operator.
H-F	Hartree-Fock
H-K	Hohenberg-Kohn Theorem
HSE	Heyd-Scuseria-Ernzerhof
KE	Kinetic energy
K-S	Kohn Sham Theorem
LDA	Local Density Approximation
m_e	Mass of an electron
$N:TiO_2$	Nitrogen doped Titanium dioxide
n(r)	Electron density
NCPP	Norm-conserving pseudo-potential
PBE	Perdew–Burke–Ernzerhof functional

PBEsol   Enhanced Perdew–Burke–Ernzerhof functional
                for solids

PBE0   Perdew-Burke-Ernzerhof hybrid

Pdos   Projected density of states

PP   Pseudo-potentials

PW91   Perdew-Wang functional

P-samples   Samples of nitrogen substitution into Ti_2O_3
                primitive cells

QE   Quantum ESPRESSO

Ry   Rydberg units (13.6 eV)

S- samples   Samples of nitrogen substitution into Ti_2O_3 in
                hexagonal convectional cells

SC   Self-consistence

SCF   Self consistent field

T   Kinetic energy

Ti_2N_2O Titanium oxynitride

Ti_2O_3 Titanium sesquioxide /Titanium (III) Oxide

TiO_2 Titanium dioxide

USPP   Ultra-soft pseudo-potential

VB   Valence Band

VBM   Valence Band Maximum

V_{e-e} Mutual electron-electron potential energy

$V_{eff\,(r)}$ Effective potential

V_{ext} Exchange-correlation potential

$V_{ext\,(r)}$ External potential

V_H Hartree term

V_{n-e} nucleus –electron potential energy

V_{n-n} nucleus-nucleus potential energy

V_{xc} Exchange Energy

XC   Exchange –correlation.

XcrysDen	X-Window Crystalline Structure and Densities
∇_I^2	Laplace operator for nuclei
∇_i^2	Laplace operator for electrons
Ψ	many-body wave function,
ε	The permittivity of vacuum

CHAPTER 1: INTRODUCTION

1.1: Background of the Study

Titanium-based oxides have attracted considerable attention due to their widespread use in photovoltaics and photocatalytic water treatment (Wu *et al.,* 2013), thus the need for a better understanding of their properties. Water is arguably the most important natural resource, accounting for around 70% of the surface of the earth (Cunningham and Saigo, 1995). Due to significant population growth, the demand for water has increased, resulting in a water shortage. Water contamination has also risen dramatically as a result of rapid industrial growth and urbanization, causing disease and death (Foundation, 2014). Photo-catalysis remains a potentially low-cost and effective water treatment mechanism (Asahi *et al.,* 2001). Figure 1.1 displays the photo-catalyst process, in which solar energy interacts with a semiconductor to absorb a photon. The photon excites an electron that causes a redox reaction where the hydrogen ion reacts with water to produce hydroxyl radicals and the oxygen reacts with electrons to generate powerful super-oxides responsible for the degradation of pollutants.
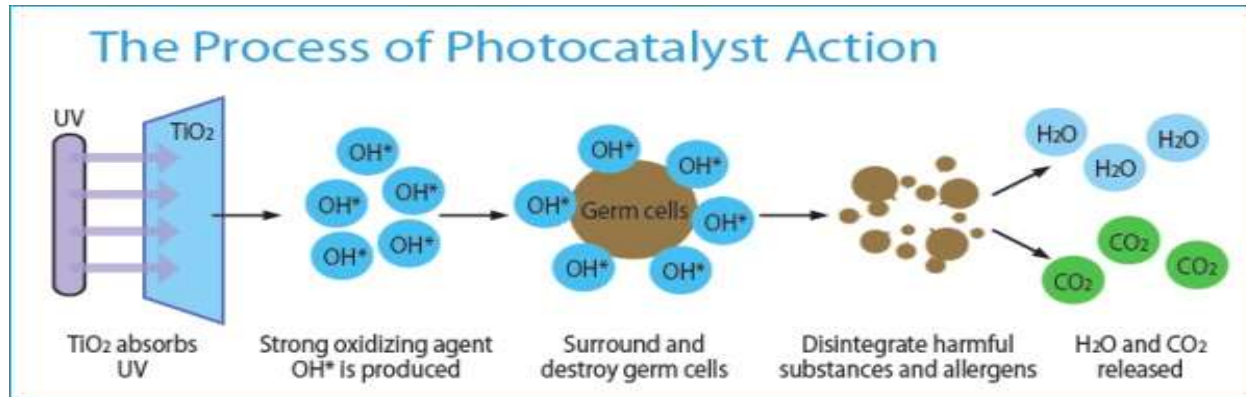
Figure 1.1: The process of photocatalytic action (Gnanaprakasam *et al.,* 2015).

Nanomaterials made of titanium dioxide (TiO_2) have applications ranging from basic products like sunscreen to complex technology like photovoltaic cells, among others (Chen and Selloni, 2014; Le Bahers *et al.,* 2014). Solar cells are recommended over fossil fuels such as gas and coal because they serve to counter global warming resulting from the combustion of fossil fuels (Guo *et al.*, 2011).

TiO$_2$ is an auspicious and highly versatile material, except for its wide bandgap which limits it to utilize only about 4% of the solar energy (Morikawa *et al.,* 2001). Band gap reduction has proved to enhance the photo-activity of TiO$_2$ for improved solar energy applications (Morgan and Watson, 2010). Doping has been suggested as a potential means of bandgap narrowing (Mahendra *et al.,*2019) . Doping is the process of adding impurities to a substance in order to change its characteristics. Nitrogen substitution into the TiO$_2$ structure has demonstrated an improved optical absorption (Mahendra *et al.,* 2019), but the probability of doping higher oxide phases of Titania has not been adequately investigated. In this work, *ab-initio* studies have been employed.

1.2: Electronic Structure Calculations using *ab-initio* Studies

Numerical solutions to the Schrödinger equation (Schrödinger, 1926) are required for computing the electronic structure of a given system. These electrical structure computations differ from other modeling methods in that they are based on fundamental principles, also known as *ab-initio* (Muscat *et al.,* 2002). That is, they do not have any external parameters apart from the most basic system definition. To study the properties of materials, first-principles measurement employs the fundamental laws of physics (Hohenberg and Kohn, 1964). Many investigations in the area of condensed matter have been made feasible thanks to the use of first-principle calculations in identifying newer materials and providing a complete explanation of experimental data.

Several theories have been developed in the study of the behavior of materials, from Hartree to Hartree-Fock (Kohn and Sham, 1965), which has no approximation except that it neglects electron-correlation, to Density Functional Theory (DFT) (Kohn and Sham, 1965). The growth of *ab-initio*-based computational work is also attributed to the rapid advancement of computer technology. Given this, the structural and electronic calculations of the Titania-based oxides, which have received both experimental and theoretical attention, as well as the least studied Corundum Ti$_2$O$_3$ and oxynitride Ti$_2$N$_2$O have been studied using DFT (Hohenberg and Kohn, 1964). In order to enhance band gap prediction from local GGA calculations, the Hubbard U term has been used. The U range has been chosen from 1 to 7 eV to investigate how these U parameters boost the energy band gap approximation of TiO$_2$ and Ti$_2$O$_3$ within each exchange-correlation functional. The Hubbard U's major goal is to correct for self-interaction effects of the d and f states, which

appear to be too close to the Fermi energy (Goh *et al.,* 2017). On Ti-3d states, the U was applied. Nitrogen partial substitution in the parent Ti_2O_3 structure was used to model oxynitride (Ti_2N_2O).

1.3: Statement of the Problem

Rutile and anatase phases of TiO_2 have bandgaps which range from 3.0 to 3.2 eV (Asahi *et al.,* 2001), these are too large to absorb visible light, necessitating the formation of an absorbance tail in the visible-light region in order to increase photoactivity. In search of Ti-based oxides with relatively narrow band gaps and better absorption thresholds, the theoretical predictions of the properties of pristine TiO_2, N: TiO_2, Corundum Ti_2O_3, and Oxynitride Ti_2N_2O have been investigated in this study. Adequate theoretical predictions are needed to promote a thorough understanding of these materials for appropriate applications.

1.4: Objectives

1.4.1: Main Objective

The main objective was to investigate the structural and electronic properties of Titanium Dioxide (TiO_2), Nitrogen doped Titanium Dioxide (N: TiO_2), Titanium Sesquioxide (Ti_2O_{2n-1}, n=2), and Titanium Oxynitride ($Ti_nN_2O_{2n-3}$, n=2) using DFT.

1.4.2: Specific Objectives

The specific objectives were:

a) To determine the lattice parameter, bond lengths, and bond angles of Titanium Dioxide (TiO_2) and Titanium Sesquioxide (Ti_2O_3).

b) To determine the optimum doping level of nitrogen in TiO_2.

c) To assess the impact of nitrogen substitution on the structures of TiO_2 and Ti_2O_3.

d) To determine and analyse band structures and density of states of pristine and doped TiO_2 and Ti_2O_3.

1.5: Justification and Significance of the Study

As discussed in section (1.1) of this thesis, Ti-based oxides have a broad range of applications. It is important to carry out fundamental studies on their properties (e.g. the effects of doping on their structures) to reduce the discrepancy between theoretical expectations and actual material properties. Theoretical predictions tends to guide experiments, especially in cases where sample preparation is a challenge or in novel materials (Sholl and Steckel, 2011). This has been made possible by the exponential growth in computing power (Pokluda et $al.,$ 2015). There is very scanty information from the first-principle calculations on the properties of higher-oxide phases of titania like Ti_2O_{2n-1}, $n \geq 2$. This study provides information to complement the pristine TiO_2, $N:TiO_2$, Ti_2O_3, and Ti_2N_2O experimental studies.

CHAPTER 2: LITERATURE REVIEW

2.0: Introduction

A summary of what has been done with Ti-based oxides, on which this study is based, is given in this chapter. The chapter begins by explaining the significance of materials modeling and its role in the study of materials properties. This is followed by an overview of theoretical and experimental studies on Ti-based oxides. Finally, this study looked at recent studies on doping in Ti-based oxides.

2.1 Materials Modeling

Modeling is one of the key methods used in studying systems. Computational materials design aids in the application of current scientific knowledge, which has an impact on decisions that satisfy efficiency and convenience in the relevant areas of usage (Jensen and Kilin, 2012Good knowledge of the accuracy of the electronic band gap, and gap level alignment among others are critical when a material is modeled for a suitable application (Burke, 2007). A summary of previous theoretical and experimental works on Ti-based oxides is given in section 2.2.

2.2 Theoretical and Experimental Studies on Titanium Oxides

Li *et al.* (2018) examined the connection between narrow band gap Ti_2O_3 and wide-bandgap TiO_2 in which they offered a platform to explore photo electro-catalytic applications in oxide materials (Sedghi-Ghamchi *et al.,*2007). Attempts have been made to explore titanium-based photo-catalysts because of the wide range of their applications in environmental remediation and solar energy conversion (Linsebigler *et al.,*1995). In both phases of TiO_2, recent theoretical and experimental research has continued to attract interest, with research on anatase showing promising results in its function as a photocatalyst (Asahi *et al.,* 2001). Examining experimental reports for both anatase and rutile phases, Chen *et al.,* (2011) indicated that anatase is responsible for the high conversion efficiency of the photochemical solar cell.

Kuroda *et al.* (2005) studied titanium oxynitride ($TiO_{2-x}N_x$) A film of Ti_3-O_4N material was investigated and found to have a greater photocatalytic activity compared to TiO_2 film to help speed up the search for an effective process for the production of the chemicals (Hyett *et al.,* 2009). Even though titanium dioxide (TiO_2) containing Ti^{4+} has a wide band gap (Fahmi *et al.,* 1993), it

is still widely studied for catalysis and solar energy applications (Zhang and Kilin, 2012), much emphasis has not been laid on the properties of titanium sesquioxide (Ti_2O_3) containing Ti^{3+} ions and its oxynitride (Ti_2N_2O).

As for computational models, within density functional theory (DFT), standard LDA and GGA functionals improve understanding of the materials under investigation, allowing for the determination of their properties. DFT projected more stability in anatase than rutile at ground state (Muscat *et al.,* 2002), with the band gap of anatase being greater by 0.17 eV with respect to rutile (Mikami *et al.,* 2000). De Angelis *et al*. (2014) and analyzed the energy of photo-generated electrons in bulk TiO_2 using hybrid functional computations. The researchers also discovered that excitons produced by UV irradiation were trapped on (101) anatase TiO_2 surface.

The probability of enhancing the photoactivity of the higher oxide phases of TiO_2 has not been adequately studied. However, considering the lack of correction of self-interaction in DFT studies (Hohenberg and Kohn, 1964), the electrons of d and f states can present problems when it comes to compounds of transitional elements. To decrease Coulomb repulsion, some methods such as hybrid-functional DFT or DFT with Hubbard U correction (Samat *et al.* 2016), may eliminate these deficiencies from LDA and GGA. The hybrid functionals can provide predictions closer to the gaps presented in experiments, however, these require a lot of computational resources (Paier *et al.,* 2006). The DFT+U method utilizes lesser computational effort hence a suitable alternative when dealing with the exchange-correlation functional.

Morgan and Watson (2010) conducted investigations on oxygen vacancies and titanium interstitials via DFT+U to account for the difference in defect characteristics in rutile and anatase TiO_2. Zhu *et al*. (2014) suggested a possible band gap modification on the TiO_2 nanotube structure as opposed to the bulk material by employing the DFT+U method so as to deal with the DFT problem. Similarly, Stausholm *et al*. (2010) reported on the DFT+U (U = 5 eV) analysis of defects in bulk rutile after performing calculations which ended up in spatially located gap states around the Ti atoms. Major attempts have also been employed in studying doping in TiO_2 with varying degrees of success as outlined in section 2.3.

2.3: Doping in Titania based Oxides

As observed by Mrowetz *et al.* (2004), the practice of doping is an important means of controlling the photoactivity of TiO_2 via the introduction of different elements into its lattice. Doping with anions or cations of a semiconductor contributes to various electronic properties (Martyanov *et al.,* 2004). Doping may be interstitial or substitutional, typically carried out using atoms with smaller ionic radii (Santara *et al.,* 2013).

Asahi *et al.* (2001), Chen and Burda (2008), Lindgren *et al.* (2003), Di Valentin *et al.* (2007), and Mrowetz *et al.* (2004) among other researchers' have put much effort in developing an understanding of doping in TiO_2, with candidate dopants such as N, F, C, P, H, S, and V. The mixing of p states from N and O was found to be significant in reducing the band gap size in N: TiO_2. This result is similar to what is reported for S doping. A more detailed analysis of doping with non-metals is present in the reviews of Chen *et al.* (2011), Fujishima *et al.* (2008), and Etacheri *et al.* (2015). Filippone *et al.* (2009) and Mo *et al.* (2015) studied H impurity defects in rutile TiO_2 and reported that H in rutile exist as O-H complexes. An additional experimental report by Mo *et al.*(2015), shows that the introduction of H changes the electronic structure indirectly through the induced change in different orbitals.

Further work on doping with metals exists (Mulmi *et al.,*2004; Ravishankar *et al.,*2016; Richter *et al.,*2005; Roca *et al.,*2015; Wu *et al.,*2017) with varying levels of success and agreements. Mulmi *et al.* (2004) reports, based on chemical vapour decomposition, showed that shallow levels appear on doping anatase with Nb, ascribing these levels to d-d transitions. Later work by Mo *et al.* (2015), however, was in agreement on the TCO like the behavior of Nb-doped anatase. These reports indicate that doping anatase with Nb leads to metallicity in anatase. Wu *et al.* (2007) reports however that the doping of anatase with Nb does not lead to increased performance as a visible light photo-catalysts, a development that introduces more need for greater understanding of the physics of the photo-activation after doping, and most importantly, developing a robust understanding of the changes the dopant makes to the structure of TiO_2. At Ti sites in TiO_2, Henderson *et al.* (2003) doped various cations such as Ni, Fe, Mn, Cr, and V; such cationic doping resulted in reduced photocatalytic activity as a result of the additional states formed within TiO_2 band gap, which would act as recombination centres for photo-excited electrons.

An anion (S, B, N, and C) doping in TiO_2 resulted in the p-state moving closer to the valence band, intrinsically TiO_2 are n-type semiconductor (Fujishima *et al.,* 2008; Sakthivel and Kisch, 2003; Schneider *et al.,* 2014). In the anatase TiO_2 crystal, C, N, F, P, and S elements have been substituted with oxygen for better photo-catalysis (Asahi *et al.,* 2001). The p-states lead to a decrease in band-gap by entangling with Ti-3d states, hence N doped structures were more efficient. Doping with nitrogen was reported to extend the onset of absorption of light from 380 nm to a range of 400 nm to 700 nm and to have potential visible light irradiation catalytic performance (Asahi *et al.,* 2001; Sakthivel and Kisch 2003; Fujishima *et al.,* 2008). Doping with S showed a reduction of the band-gap, but incorporating it into the TiO_2 crystal was a challenge because of its wider ionic radii (Asahi *et al.,* 2001). These and many more studies have succeeded in doping metals into TiO_2 photo-catalysts to obtain visible light photo-response (Schneider *et al.,* 2014).

Aoki *et al.* (2019) described the electronic properties of TiO_2 and Ti_2O_3 within DFT formalism through GW approximations, while Wu *et al.,* (2013) carried out the theoretical prediction of $Ti_nN_2O_{2n-3}$ solid compounds for the n = 3 case ($Ti_3N_2O_3$) using a high throughput screening method within DFT. Guo *et al.* (2011) suggested that TiO_2 doped with metals is thermally unstable, and that cationic dopant electronic states can serve as carrier recombination centers, resulting in a reduction in photocatalytic performance. Furthermore, due to its ability as a material for environmental photocatalysis, N: TiO_2 has been shown to produce thermally stable N-atom impurities. (Di Valentin *et al.,* 2007; Mahendra *et al.,* 2019). Given this, TiO_2 anatase and rutile were doped with non-metal, nitrogen. The higher oxide phases of Titania and their oxynitrides were as well considered for this work. With an aim of improving the properties of the oxides, partial substitution of nitrogen atom(s) at the oxygen site(s) was performed.

CHAPTER 3: THEORETICAL BACKGROUND

3.0: Introduction

Theoretical framework, which includes density functional theory (DFT), which is the foundation for this work, is covered in this chapter. Fundamental theorems on which DFT is built are discussed in this chapter. The wave function picture of Schrödinger for particles (electrons) is considered and DFT approximations, are discussed. In this chapter, types of pseudopotentials commonly used in modeling ion cores are also outlined. Donev *et al*. (2015), Sholl and Steckel (2011), Burke (2007), and Jensen and Kilin (2012) are the primary sources of information used in this chapter. The chapter concludes with an explanation of the properties of the materials investigated in this research.

3.1: Background of Density Functional Theory (DFT) Study

Density Functional Theory started with two approaches, the Thomas-Fermi formulation which rests on the free electron gas model, and the Thomas-Fermi-Dirac model that later evolved to include electron exchange (Slater *et al.,*1935). In both cases, the electron density was key but without the concept of electron orbitals. Due to their limited accuracy, these approaches were discarded.

3.1.1: Density Functional Theory

Calculating electronic properties for both ground and excited states are important parts of materials science research. However, gaining a thorough knowledge of these electronic properties is difficult. It's crucial to understand how materials behave. Electrons and nuclei determine most features in condensed matter systems thus providing the required information about bulk, magnetic, electrical, and optical properties (Lykos and Pratt, 1963). A lot of research is still ongoing on many theories of the method. A solution to Schrödinger equation can be obtained in a set of interacting electrons in an external Coulomb field.

The time-independent non-relativistic Schrödinger equation is given by;

$$H\psi=E\psi, \tag{3.1}$$

Hamiltonian operator is H, E denotes the system's total energy, and the many-body wave function is denoted by ψ. Because the Hamiltonian has a simple form, for a particle in a box, the Schrödinger equation can be solved. Multiple electrons interact with multiple nuclei in the many-body problem (Burke, 2007). The position of each electron and nucleus in the system determines the many-body wave function ψ. For a system of a number of electrons and nuclei, the wave function for many bodies is given by (Sholl and Steckel, 2011);

$$\psi = \psi\,(r_1, r_2, \ldots r_N; R_1, R_2, \ldots, R_M). \tag{3.2}$$

The sum of potential and kinetic energy operators is the Hamiltonian operator. The kinetic energy operator, denoted by T is given by (Sholl and Steckel, 2011) ;

$$T = -\sum_{i=1}^{N} \frac{\hbar^2}{2m_e} \nabla_i^2 - \sum_{I=1}^{M} \frac{\hbar^2}{2M_I} \nabla_I^2 \,, \tag{3.3}$$

where $\hbar$ is reduced Plank's constant, $\nabla_i^2 \, and \, \nabla_I^2$ is Laplace operator, the mass of an electron is denoted by m_e, while M_I is the mass of the Ith nucleus. The Laplace operators for electrons and nuclei are given by $\nabla_i^2 = \frac{\partial^2}{\partial x^2} + \frac{\partial^2}{\partial y^2} + \frac{\partial^2}{\partial z^2}$, and $\nabla_I^2 = \frac{\partial^2}{\partial X^2} + \frac{\partial^2}{\partial Y^2} + \frac{\partial^2}{\partial Z^2}$, respectively.

For potential energy, the Coulomb repulsion between electron pairs given by (Sholl and Steckel, 2011);

$$V_{e-e} = \frac{1}{2} \sum_{i \neq j} \frac{e^2}{4\pi\varepsilon_o} \frac{1}{|r_i - r_j|} \,, \tag{3.4}$$

where the electron charge is denoted by *e,* the electron coordinates, r_i and r_j, and, the permittivity of vacuum ε_o. *i* and *j* are indices that range from 1 to N since an electron can only repel another electron and not itself the term *i=j* is exempted, and we divide by 2 to take care of the double counting corrections (Giustino, 2014).

Coulomb repulsion between nuclei is given by (Sholl and Steckel, 2011);

$$V_{n-n} = \frac{1}{2} \sum_{I \neq J} \frac{e^2}{4\pi\varepsilon_o} \frac{Z_I Z_J}{|R_I - R_J|} \,, \tag{3.5}$$

where indices *I* and *J* range from 1 to M, Z represent atomic numbers with R_I and R_J being nuclei coordinates.

Coulomb attraction between electrons and nuclei is given by (Sholl and Steckel, 2011);

$$V_{n-e} = -\sum_{i,I} \frac{e^2}{4\pi\varepsilon_o} \frac{Z_I}{|r_i - R_I|} . \qquad\qquad\qquad . \quad (3.6)$$

Where the indices i range between 1 and N while I range between 1 and M, Z_I represents atomic number.

The many-body Schrödinger equation is obtained as a combination of the equations for potential and kinetic energy, as indicated in equation (3.7) (Sholl and Steckel, 2011);

$$\left[\begin{array}{c} -\sum_{i=1}^{N} \frac{\hbar^2}{2m_e} \nabla_i^2 - \sum_{I=1}^{M} \frac{\hbar^2}{2M_I} \nabla_I^2 + \frac{1}{2}\sum_{i\neq j} \frac{e^2}{4\pi\varepsilon_o} \frac{1}{|r_i - r_j|} + \frac{1}{2}\sum_{I\neq J} \frac{e^2}{4\pi\varepsilon_o} \frac{Z_I Z_J}{|R_I - R_J|} \\ \\ -\sum_{i,I} \frac{e^2}{4\pi\varepsilon_o} \frac{Z_I}{|r_i - R_I|} \end{array} \right] \psi = E\psi, \qquad (3.7)$$

For electrons and nuclei, the kinetic energy operators are represented by the first two terms of the equation (3.7). The third, fourth, and fifth terms, respectively, are electron- electron repulsion, nuclei-nuclei repulsion, and electrons-nuclei attraction. N denotes number of interacting electrons and M are those of interacting nuclei, the electron charge is denoted by e, $\hbar$ represents the reduced Plank's constant, $\nabla_i^2 \ and \ \nabla_I^2$ are Laplace operators for electrons and nuclei, the mass of an electron is denoted by m_e, while M_I is the mass of the Ith nucleus. r_i and r_j are the electron coordinates, Z_I represents atomic numbers and ε_o is the permittivity of vacuum. Indices that range from 1 to N are denoted by i and j, since an electron can only repel another electron and not itself the term $i=j$ is exempted.

 Solving equation (3.7) would allow us to obtain a given system's ground state energy, which is key in determining the properties of the materials. The equation is only effective for small atoms and molecules, but difficult for large structures, for example, if we consider one molecule of CO_2, the full wave function would be given by the number of electrons multiplied by three dimensions, resulting in a 66-dimensional function that will be a problem to address. It is common to implement the Born-Oppenheimer approximation as a first approximation (Burke, 2007), where one neglects the contribution of the nuclei to the kinetic energy, as they are normally several thousand times heavier than electrons. As such, the Hamiltonian lacks the nuclei's kinetic energy operator, this leads to equation (3.8),

$$\left[-\sum_{i=1}^{N} \frac{\hbar^2}{2m_e}\nabla_i^2 + \frac{1}{2}\sum_{i \neq j}\frac{e^2}{4\pi\varepsilon_o}\frac{1}{|r_i - r_j|} - \sum_{i,I}\frac{e^2}{4\pi\varepsilon_o}\frac{Z_I}{|r_i - R_I|}\right]\psi = \mathrm{E}\psi. \qquad (3.8)$$

In solving equation (3.8), one is still faced with an unsolvable problem despite this approximation. As a result, more approximation techniques have been developed, which can be classified generally as wave-function-based or density-based (Burke, 2007). DFT is computationally essential in analyzing and predicting properties of the material. The theory articulates that electron density is the relevant physical quantity for any ground state system. Several scholars have successfully used DFT to describe numerous properties of materials because of its ability to study systems of infinite sizes whether periodic or non-periodic (Belogolova and Sidorkin, 2004; Hu and Metiu, 2011; Khan *et al.,* 2013; Kroll, 2005; Samat *et al.,* 2019). When it comes to defining system behavior, density functional theory has limitations in defining the behaviour of some systems. Even though there have been recent advancements, in correlated systems and insulators, band gaps are known to be underestimated by DFT.

DFT is built on Kohn and Sham theorems (Burke, 2007; Sholl and Steckel, 2011) that state,

- The Schrödinger equation's ground-state energy is a unique function of electron density.
- The electron density that corresponds to the complete solution of the Schrödinger equation is the actual electron density that minimizes the energy of the overall function.

According to the first theorem, wave function and electron density, both at ground state, maps on each other (Burke, 2007). This means that the system's observables are all determined in a different way by the ground-state density. It is not possible for two ground states $H\psi = E\psi$ and $H'\psi' = E'\psi'$ to give the same electronic density $n(r)$. The ground state ψ which is depends on the potential $V(r)$ and another potential $V'(r)$ of the ground state density ψ' since they are determined by different Schrödinger equations, not unless the two potentials are identical. The potential a discrete function of the density; the ground-state density determines the Hamiltonian. With this theorem, one moves from an intractable problem of 3N variables (the Schrödinger equation) to a problem with three spatial dimensions, which is in principle solvable. The theorem does not, however, state how this ground-state density and mapping can be constructed, but only proves its formal existence.

The second theorem shows an important feature of the ground state density, and an indirect means of determining the correctness of the ground state energy (Burke, 2007). One could obtain the ground state density and energy, as well as perform the minimization of the energy for the density if the form of functional dependency of ground-state total energy is given. The form of this functional dependency, however, is not given by the theorem. Hohenberg-Kohn and Kohn-Sham theorems are two very essential theorems at the core of DFT.

3.1.2: The Hohenberg-Kohn Theorem

In 1976, Hohenberg and Kohn established that density can be computed for a set of interacting particles in an external potential, V_{ext} (r), in such a way that V_{ext} (r), is a defined functional of the density, which is heavily acknowledged in DFT (Hohenberg and Kohn,1976). According to Sholl and Steckel (2011), ground state energy is a unique function of electron density. The actual ground-state electron density is the one that significantly reduces the overall functional energy (Burke, 2007).

3.1.3: Kohn-Sham Equation

The Schrödinger equation for non-interacting particles, which is non-existent, produces the same density a given system of interacting particles (Burke, 2007; Sholl and Steckel, 2011). Kohn and Sham reorganized the many-body problems in a detailed and familiar way that strengthened the functional applications of DFT (Hendrik, 1976). The Hamiltonian is structured in a way that it has the same ground-state density as the interacting system. The electronic density, ground-state energy, and other desired observables can easily be obtained, given an external potential with the only impediment being the exchange-correlation term (Burke, 2007; Sholl and Steckel, 2011).

In atomic units, where $\hbar = m_e = e = 1$,

$$V_{eff} = V_{ext} \text{ (r)} + V_H [\text{n (r)}] + V_{xc} [\text{n (r)}], \tag{3.9}$$

V_{eff}(r) denotes the effective potential, the second term the external potential V_{ext}, V_H -Hartree term, V_{XC} -exchange-correlation term and, n (r) denotes electron density. The solution to the K-S equation (3.10) is the key solution in computational methods.

$$H\psi_i(r) = \left[\frac{-1}{2}\nabla_i^2 + V_{eff}(r)\right]\psi_i(r) = \varepsilon_i \psi_i \text{ (r)}. \tag{3.10}$$

H denotes the Hamiltonian operator, $V_{eff}(r)$ the effective potential, ε_i the minimum energy and, ψ the many-system wave function.

The K-S equation is solved with fixed-point iteration, though the initial input for n(r) is usually a guess. The self-consistent field (SCF) approach iterates the input until n(r) and the output n'(r) appears identical within the energy cutoff limit.

3.1.4: The Self-Consistent Field (SCF) Cycle

kinetic energy operator and the effective potential, $V_{eff}(r)$, constitutes the Hamiltonian Operator H as shown in equation (3.9). V_{eff} is dependent on n (r) and can be calculated from ψ_i. However, ψ_i is reliant on $V_{eff}(r)$ and hence n (r). The flow chart in Figure (3.1) depicts the process in its entirety. The flowchart below demonstrates how to calculate the Kohn-Sham equations for a bunch of frozen nuclei (ions). With Cutoff energy optimized and k-points sampled, the trial density is chosen by defining the cutoff of the charge density (ecut 'rho') which also dictates the type of pseudopotential to be used.

The calculated density is then applied as an input for derivation of V_{xc}. As seen in equation (3.11), the efficient potential, $V_{eff}(r)$, is the product of external potential V_{ext}, Hartree term V_H, and exchange-correlation term $V_{xc}(r)$. The system's Hamiltonian is equivalent to $V_{eff}(r)$ + K.E. The guessed electron density n (r) is the initial density.

$$n\ (r) \propto E_0, \tag{3.11}$$

n (r) denotes the electron density and E_0 ground state energy, the estimated and calculated densities are consistent, implying that they are self-consistent. The energy, forces, and other parameters can then be determined. If the estimated and calculated densities differ, a further density estimate based on the electron density is made from the previous step, unless self-consistency is obtained, the whole process is repeated. The schematic diagram showing the self-consistency scheme is presented in Figure 3.1.

The flowchart contains the following boxes:

Initial guess for n (r)

use n (r) to calculate V_{eff} (r)

$$V_{eff} (r) = V_{nuc} (r) + \int \frac{n (r')}{|r-r'|} dr' + V_{xc}[n(r)]$$

Solve Kohn- Sham equation

$$\left[\frac{\hbar^2}{2m_e} \nabla_i^2 + V_{eff}(\boldsymbol{r}) \right] \Psi_i = \varepsilon_i \psi_i$$

new n' (r)

$$n'(r) = \sum |\psi i(r)|^2$$

Self-consistent?

No

Yes

Generate new n (r)

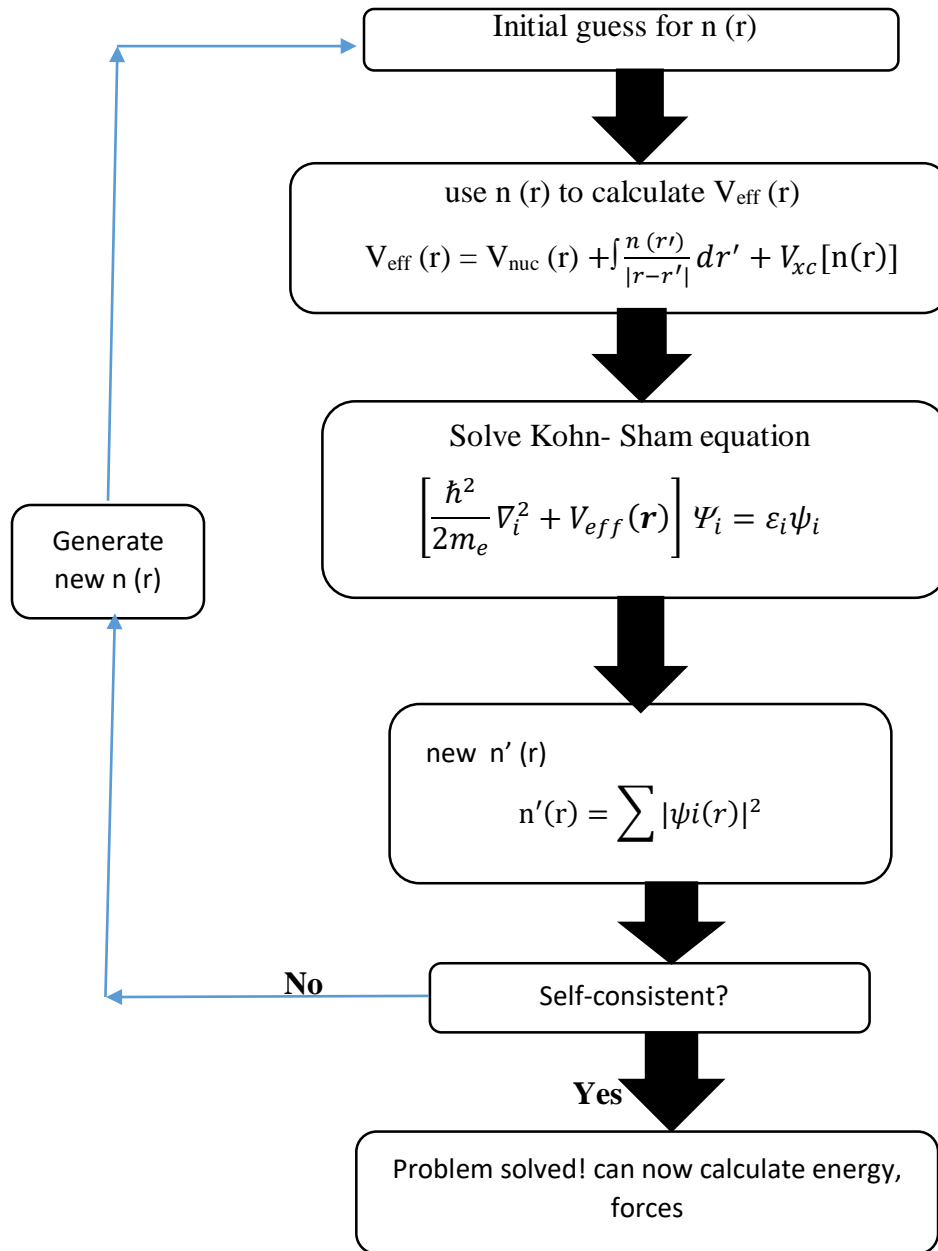**Problem solved! can now calculate energy, forces**

Figure 3.1: Schematic diagram showing the self-consistency scheme   (Shan *et al.*, 2017)

3.1.5: Approximation for the exchange-correlation energy

Finding the Schrödinger equation's ground-state energy in many-body problems is extremely challenging. The problem relates to the fact that when solving Kohn-Sham equations, the exchange-correlation functional should be defined. The Hohenberg-Kohn theorem guarantees the presence of the actual form of exchange-correlation, but its exact nature is unclear. Conveniently, the electron density does not fluctuate at all points in space in this scenario, the functional can be obtained from uniform electron gas. In any real material, this case can tend to be of limited value because the variation in electron density determines the chemical bond that makes a material. The uniform electron gas provides a realistic approach of employing the Kohn-Sham equations. Local Density Approximation (LDA) and Generalized Gradient Approximation (GGA) are two basic exchange-correlation functionals (Burke, 2007). LDA +U, GGA+U, and hybrid fuctionals are also in use.

3.1.5.1: Local Density Approximation (LDA)

The local density approximation (LDA) refers to the estimation of exchange-correlation functional using the local density. Since the exchange-correlation functional used is not exact, the LDA supports the entire description of K–S equations, even though the results do not solve the real Schrödinger equation accurately. (Sholl and Steckel, 2011).

3.1.5.2: Generalized Gradient Approximations (GGA)

The generalized gradient approximation (GGA) contains additional physical information compared to LDA. (Sholl and Steckel, 2011). Thus, relative to LDA, it is considered to be more accurate most systems. The information from the electron density gradient are mimicked in a GGA functional in a variety of ways, which is why there are so many distinct GGA functionals used in solids calculations, such as the Perdew-Wang functional (PW91), the Perdew-Burke-Ernzerhof functional (PBE), and enhanced Perdew-Burke-Ernzerhof functional for solids (PBEsol) (Sholl and Steckel, 2011). Other GGA functionals, such as GGA+U, have been designed and are currently in use. In this work, enhanced Perdew-Burke-Ernzerhof functional for solids (PBEsol) has been used.

3.1.6: Density Functional Theory with Coulomb interaction (DFT + U)

The DFT+U approximations is designed to improve the description of correlated systems' ground state (Dorado *et al.*, 2009). The Hubbard model influenced this technique. The DFT+U falls within the realm of DFT, requiring little work to incorporate into current DFT codes.

The primary function of the U correction is to add an additional Hubbard-like component to Coulomb interaction of electrons that are localized. The Hubbard Hamiltonian defines the electronic state of d and f orbitals, whereas typical DFT approximations are used for the rest of the valence electrons.

$$E_{DFT+U}[n] = E_{DFT}[n] + E_U[n_i^\sigma] - E_{dc}[n_i^\sigma] \qquad (3.12)$$

The overall energy (E_{DFT+U}) is the sum of GGA energy (E_U) that has an effect on each electron of spin σ at point i as calculated from equation (3.12). Due to the additive Hubbard factor; a "double-counting" component (E_{dc}) must be subtracted from the GGA's total energy because of the existing double counting error.

The DFT+U approach was used in this work by including the U on Ti -3d orbitals. In section 5.3, the effect of increasing U values on lattice parameters and bandgaps were documented and examined.

3.1.7: Pseudopotentials Technique

Several approximations are applied to practical solutions of the self-consistent (SC) Kohn-Sham (K-S) equation. Different approximations were therefore designed to be cost-effective, leading to rapid convergence, caution was taken not to compromise the calculation of results. The *ab-initio* pseudo-potentials (PP) technique involves valence electrons thus making the calculations relatively cheaper (Ashcroft and Mermin, 1976b). The inner core states, as well as the strong potential that binds them to the positive nuclei, are neglected in contrast to the whole potential method (Jensen and Kilin, 2012). Ion cores have a minor impact on solid characteristics, despite the fact that included them in pseudo potentials increases the use of plane wave basis sets in the calculations.
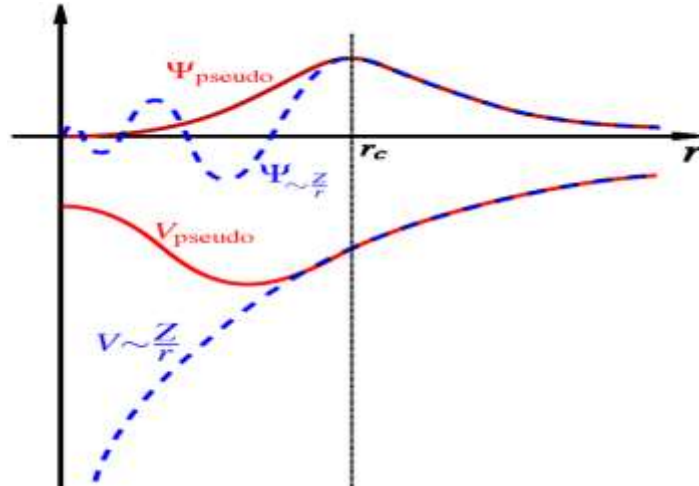
Figure 3.2: Pseudo and real-potentials at a specific cut-off radius, rc (Vanderbilt, 1990).

The pseudo-potential (red) and the wave-function of the Coulomb potential of the nucleus (blue) agree at a certain cut-off radius, rc as seen in Figure 3.2. Ultrasoft Pseudopotential (USPP) and Norm Conserving Pseudopotentials (NCPP) are the main types of pseudopotentials utilized in electronic structure computations.

3.1.6.1: Norm-Conserving Pseudo-Potential (NCPP)
Since mobility of core electrons is not regular, the core electrons are simplified. Normalization renders the electron movement periodic to have a Gaussian distribution that allows for quicker convergence. The charge density cut-off (ecut 'rho') is set to its default value when employing these pseudo-potentials. If it is lowered or raised, it generates instability in the system, especially on the forces and stresses (Ashcroft and Mermin, 1976b).

3.1.6.2: Ultra-soft Pseudo-Potential (USPP)
The electron distribution in the core is Gaussian initially, resulting in calculations of many plane waves. The Ultra-Soft Pseudo-Potential (USPP) implementation decreases the number of plane waves, resulting in faster convergence. USPP provides quicker convergence than norm-conserving pseudo-potentials (Ashcroft and Mermin, 1976b). It is necessary to use a value higher than the default charge density cut-off value (ecut 'rho') when using this pseudopotential. Inner shell electrons are often positioned around the ion and do not contribute to covalent bonds (Chung *et al.,* 2016). A pseudopotential that mimics the effects of a nucleus potential that is screened by its

inner electrons is therefore used instead of a physical potential for the nucleus as well as the inner electrons. USPP was used in this research to model the core electrons.

3.2: Materials properties

Computational materials design is vital in addressing several problems since it provides significant structural and electronic properties of atoms which are the basic unit in materials (Jensen and Kilin, 2012).

3.2.1: Structural properties

One of the points of interest when studying structural properties of systems is the dimensions of a unit cell, which is also referred to as lattice constant. Bond lengths and bond angles are also essential structural characteristics of a material. The bond dissociation energy is directly proportional to the bond strength, for instance, a long bond is a weaker bond compared to a shorter one (Niu, 2016) . The bond angle determines the arrangement of a molecule's atoms in space and defines the characteristics of many materials (Chung *et al.,* 2016).

3.2.2: Electronic properties

The study focuses on the band structure theory of materials and its effectiveness in describing the physical properties of solids that form the basis of understanding of an all-solid-state system (Ashcroft and Mermin, 1976a). In solids, the electronic band structure shows the energy ranges such as band gaps or forbidden gaps (Ashcroft and Mermin, 1976a). Electrons occupy atomic orbitals in a single isolated atom, with each orbital having a distinct level. The atomic orbitals overlap when atoms join. In a molecule, two electrons cannot have equal quantum numbers (Pauli exclusion principle). As a result, each atomic orbital splits into two different energy molecular orbitals when two identical atoms create a diatomic molecule, making the electrons from previous atomic orbitals to take up a new orbital structure without having to share their energy.

Chemical bonding and band formation are both aided by the presence of valence electrons in an atom. Band gaps are energy ranges in which no band can fill. The size of the band gaps varies depending on the degree of atomic orbital overlap (Harrison *et al.,*2004). Materials are often classified as conductors, insulators, or semiconductors based on the magnitude of their band gaps.
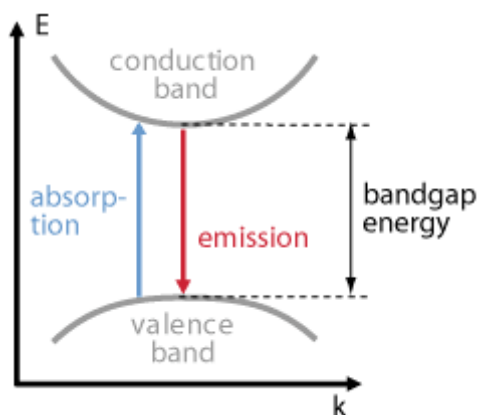
Figure 3.3: Conduction and Valence bands of a direct bandgap semiconductor (Chakraborty, 2009).

The conduction band is located on the top of the band gap, while the valence band is located on the bottom of the band gap (see Figure 3.3).

Band theory can only be used to describe solids made up of an enormous number of same atoms or molecules which are chemically combined. It approximates the quantum state of a solid. A piece of material is assumed to comprise an enormous sum of atoms for the band theory to be valid. The bands are assumed to be continuous. The structure of the band is an inherent characteristic of a material with the assumption that the material is homogeneous. Band structure also describes single-electron states, whose existence assumes that electrons travel without interacting with lattice vibrations in a static potential, as well as other electrons and photons (non-interactivity) (Ashcroft and Mermin, 1976b). One of the drawbacks of in-homogeneities and interfaces is because the bulk band structure is disturbed near surfaces and junctions (Harrison, 2004). Besides, KS- DFT bandgap will always be underestimated and what we obtain is the difference between the LUMO (lowest unoccupied orbital) and the HOMO (highest occupied orbital).

CHAPTER 4: METHODOLOGY

4.0: Introduction

This chapter has details on how simulations on pristine TiO_2, N: TiO_2, corundum Ti_2O_3, and Titanium Oxynitride Ti_2N_2O were carried out. In Appendix A of this thesis, a more detailed process of obtaining the optimized parameters is provided. Giannozzi *et al.* (2009), Hu and Metiu, (2011), and Samat *et al.* (2016) are the main references used in this chapter.

4.1: Computational Methodology

All calculations were done within DFT-GGA using the Quantum Espresso code (QE) (Giannozzi *et al .,*2009). Materials such as crystalline solids and surfaces within the DFT formalism can be simulated using the code. This study has been carried out using the *ab-initio* pseudo-potential plane wave method as mentioned earlier. Ultrasoft pseudopotentials drawn from the 2.0.1 version of Dal Corso *et al*, library (Hu and Metiu, 2011), have been used to describe the electron-ion interactions; the pseudopotential files are provided in Appendix C of this thesis.

For the exchange-correlation interaction, GGA with PBE and GGA-PBEsol have been employed. These exchange-correlations were chosen because no adjustable parameter was required hence computationally efficient. The first-principle calculations using the DFT+U method (Samat *et al.*, 2016) was also implemented. By adjusting the effective U values in the range of 1 to 7 eV, the desired U for the computations was acquired. For the Ti atom, the valence states were 3s, 3p, 3d, 4s, and 2s, 2p for both N and O atoms. Crystal structures were relaxed at T=0K and P=0 GPa and convergence tests were carried out.

4.2: Structural Optimizations

Experimental lattice parameters were considered as the starting point in the optimization of the lattice parameters. The data were integrated to the Birch-Murnaghan equation of state (Lazzeri *et al .,* 2001) with the required lattice constant obtained as the minimum value of the fitted curve. Xmgrace was used to plot the values of lowest energy acquired with their respective k-point grids (Turner, 2005). The lattice parameters and k-point meshes were set to their optimal values, then the cutoff energy was altered from 20 Ry to 80 Ry to get an optimal plane wave cutoff energies

value. The optimum values were found when the energy could no longer be changed. This was important since every system strives for a low-energy state (ground state).

4.3: Brillouin Zone Integration (K-points)

A standard technique for sampling the Brillouin zone is the Monkhorst-Pack grid (Monkhorst and Pack, 1976). Because the precision of integration is fully dependent on the integration grid used, the Monkhorst-Pack methodology (Hendrik, 1976) allows for both exact integration of sections of the Brillouin zone and sampling of the complete Brillouin zone. The Monkhorst-Pack scheme and Brillouin zone integration were used in this study to calculate band structures on converged k-point meshes. A Monkhorst-Pack grid of 4x4x6, 6x6x4, and 5x5x5 for anatase TiO_2, rutile TiO_2, and corundum Ti_2O_3 structures, respectively, were created following convergence tests for k-points with energy. Explicit positions along the high symmetry axes were described along Γ →X→ M→ Γ→ Z→ R for anatase TiO_2, Γ→ X→ R→ Z→ M→ A→ Z for rutile TiO_2, and Γ →Z→ F→ Γ →L for corundum Ti_2O_3, for band structure calculations, are indicated in Figure 4.1.

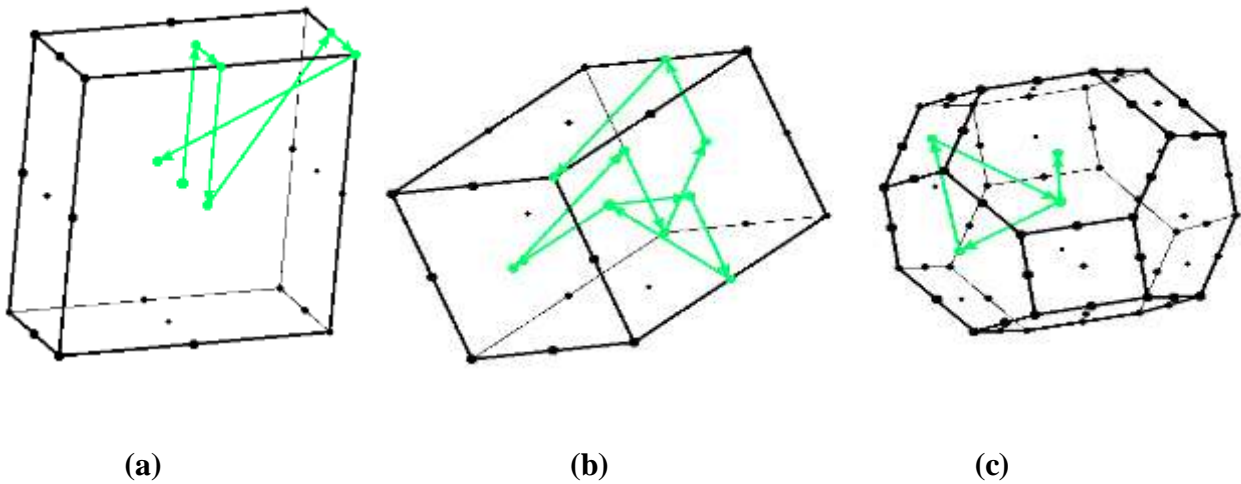| (a) | (b) | (c) |

Figure 4.1: Brillouin zone integration for (a) anatase (b) rutile, and (c) corundum Ti_2O_3, showing the origin at Γ=0

4.4: Band Structure Calculations

A defined k-points grid is necessary in determining the energy of the system. The Monkhorst-Pack approach, was used to create the special k-points in this work. The band structures of the systems are calculated by considering these high symmetry points and paths generated by the XCrysDen program (Kokalj and Causà, 2001). To account for the Ti-d interactions, the structures were subjected to a moderate Coulomb Repulsion U to adjust the estimated electronic band gap in comparison to experimental values.

CHAPTER 5: RESULTS AND DISCUSSIONS

5.0: Introduction

Results obtained from the properties (structural and electronic) of pristine and doped rutile/anatase TiO_2 as well as corundum Ti_2O_3, both at the DFT and DFT+U theory levels, are discussed in this chapter. The results of TiO_2 research are known for the rutile and anatase phases. The purpose of doing them here is to ensure that our method can reproduce known findings and is hence adequate. First, the structural parameters of the systems and the impact of the dopant on the geometry of the systems are discussed, then, the effect of the dopant on the properties of the systems are examined. Next, a variety of Ti_2N_2O samples are modeled using primitive and hexagonal convectional corundum Ti_2O_3 structures, labeling them P and S samples for primitive and hexagonal convectional cells, respectively.

At the end of the chapter, a brief discussion summarizes the work discussed in the chapter and comments on it. Aoki *et al*., (2019), Asahi *et al*., (2000), Mikami *et al.,* (2000), Morikawa *et al.*, (2001), and Samat *et al.,* (2016), are the key references used in this chapter. A detailed technical overview of the methods for this work can be found in the appendix A, B, C, and D which contains descriptions of structural optimization, the pseudopotential files, band structures, and the input files, respectively.

5.1: Structural Properties

5.1.1: Pristine Structures

The systems under study are tetragonal rutile and anatase TiO_2 with lattice parameters a=b ≠ c,α=β=γ=90° and trigonal Ti_2O_3 with a= b=c, α = β= γ≠90°. Lattice constants of the TiO_2 (anatase and rutile) and Corundum Ti_2O_3 from the two Generalized Gradient Approximation (GGA) flavors, PBE and PBEsol, are described along with the corresponding experimental values in Table 5.1.

<table>
<tr><td>(**a**)</td><td>(**b**)</td><td>(**c**)</td></tr>
</table>

Figure 5.1:   optimized structures for (**a**) anatase TiO_2, (**b**) rutile TiO_2. and (**c**) Corundum Ti_2O_3.

The calculated lattice constant 'a' using GGA-PBE and GGA-PBEsol for anatase TiO_2 is 3.75 Å and 3.77 Å, respectively, while the stated experimental value is 3.78 Å (Yang *et al.,* 2010). Consequently, the calculated lattice parameter 'a' for rutile using GGA-PBE is 4.55 Å while GGA-PBEsol is 4.63 Å. The reported experimental value for rutile is 4.64 Å (Yang *et al.,* 2010), from which it was deduced that PBEsol offers a better description of the properties of the materials than PBE. This agrees well with the results of Samat *et al.* (2019), which is why GGA-PBEsol was used for the rest of the calculations in this study. The ground-state properties of materials are significantly influenced by the choice of exchange and correlation functionals, according to this comparative study. Table 5.2 shows the bond lengths and angles that were calculated.

Table 5.1: Lattice parameters of rutile, anatase TiO_2, and corundum Ti_2O_3.

Method	Rutile TiO_2		Anatase TiO_2		Corundum Ti_2O_3	
	a_o (Å)	C (Å)	a_o (Å)	C (Å)	a_o (Å)	C (Å)
GGA-PBE (This work)	4.55	2.95	3.75	9.45	5.27	5.27
GGA-PBEsol (This work)	4.63	2.93	3.77	9.69	5.16	5.16
Other GGA-PBE	4.59 [a]	2.94 [a]	3.76 [a]	9.57 [a]	5.17 [b]	5.17 [b]
Other GGA-PBE	4.58 [c]	2.97 [c]	3.80 [c]	9.59 [c]		
Experiment	4.64 [d]	2.96 [d]	3.78 [d]	9.70 [d]	5.15 [e]	5.15 [e]

[a] Inturi *et al.* (2014) [b] Aoki *et al.* (2019) [c] Samat *et al.* (2019)
[d] Yang *et al.* (2010) [e] Li *et al.* (2018)

Table 5.2: calculated and experimental bond lengths (Å) and bond angles (degrees) for TiO_2 (anatase and rutile) and Ti_2O_3.

|	Bond lengths (Å)				Bond angles (degree)			
		Rutile TiO_2	Anatase TiO_2	Corundum Ti_2O_3		Rutile TiO_2	Anatase TiO_2	Corundum Ti_2O_3
Calculated value	Ti –O	1.96	1.96	3.85	Ti-O-Ti	131.94	155.40	85.42
					O-Ti-O	90.00	77.71	99.76
Other DFT values	Ti –O	1.96	1.98		Ti–O-Ti	131.92 [a]	156.08 [a]	
					O-Ti-O	90.00 [a]	78.07 [a]	
Experimental value	Ti –O	1.95	1.94	3.78	Ti–O-Ti	130.97 [b]	154.34 [b]	86.30 [c]
					O-Ti-O	90.00 [b]	78.67 [b]	98.41 [c]

[a] Samat *et al.* (2019) [b] Yang *et al.* (2010) [c] Li *et al.* (2018)

The calculated bond angles for TiO_2 rutile are 131.94° and 90.00°, which are on average equal to the 130.79° and 90.00° experimental values from Yang *et al.* (2010) and Li *et al.* (2018) ,

respectively. Negative deviations of slightly more than 1% are found in the anatase TiO_2 bond angle. In rutile, the calculated bond lengths and bond angles also deviate by 1.1% and 1.24%, respectively. Ti_2O_3 had deviations of 1.16% and 2.04% with respect to experimental values by Samat *et al.* (2019). The deviations are attributable to the fact that the simulations did not account for the presence of intrinsic and other imperfections that occur in real materials. Prior than that, as indicated in Table 5.2, this concur with other DFT findings by Inturi *et al.* (2014) and Aoki *et al.* (2019). In general, it was found that, while GGA functionals is poor in describing the electronic properties of these localized orbitals, they do an excellent job in describing the energy of the system and the structural properties are adequately replicated.

5.1.2: Nitrogen doped TiO₂ structures

To minimize surface effects, the substitution was done in a supercell as this study is on bulk properties. Figures 5.2 (a) and (b) show supercells for rutile and anatase TiO_2 doped with 2% nitrogen. The percentage dopant concentration was obtained by dividing the number of dopant atoms with the total number of atoms in the supercell than multiplying by 100. In the 2x2x2 rutile and 2x2x1 anataseTiO_2 supercells, each comprising 48 atoms, a nitrogen atom was substituted for an O atom.
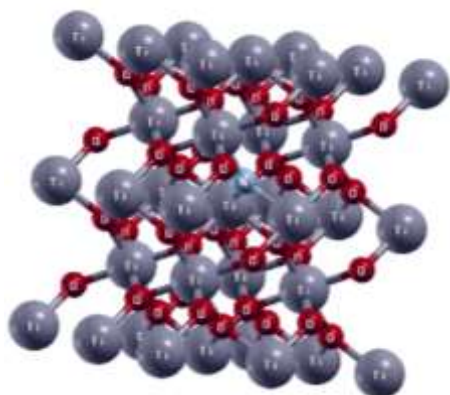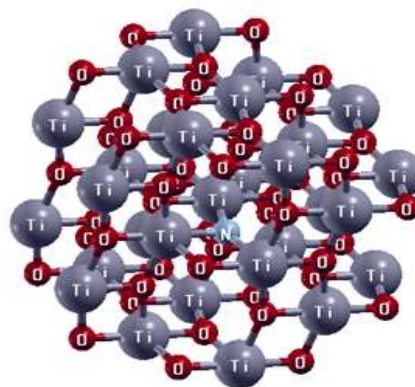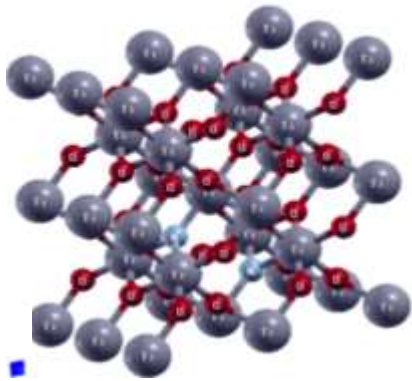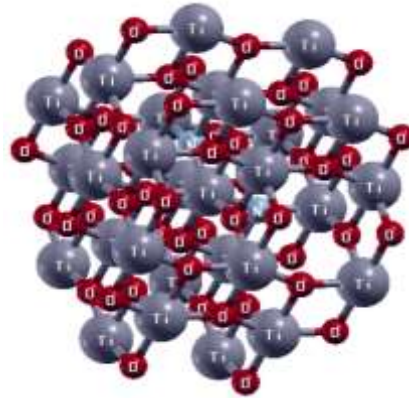

(a) Rutile   (b) Anatase

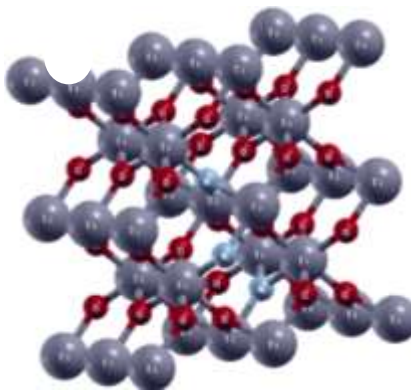**Figure 5.2:** TiO_2 doped with 2% N (a) Rutile structure (b) Anatase structure.

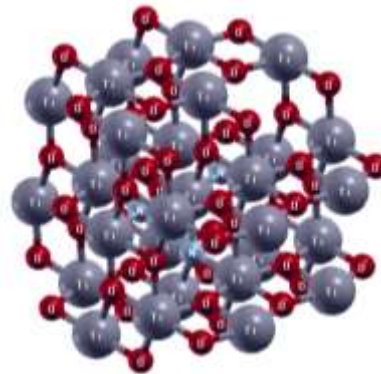(a) Rutile TiO$_2$.   (b) Anatase TiO$_2$.

Figure 5.3: Rutile and Anatase phases of TiO$_2$ after doping with 4% N at substitutional sites.

(a) Rutile TiO$_2$.   (b) Anatase TiO$_2$.

Figure 5.4: Rutile and Anatase phases of TiO$_2$ after doping with 6% N at substitutional sites.

To achieve a 2% dopant concentration, one oxygen atom was substituted with a nitrogen atom in Figure 5.2. The same was done in Figure 5.3, to reach a 4% doping level, two oxygen atoms were replaced with two nitrogen atoms. To obtain a 6% doping level, three oxygen atoms were substituted with three nitrogen atoms in Figure 5.4. The supercells were created using Phonopy software (Togo and Tanaka, 2015).

The structural properties from the relaxed doped systems were calculated and compared with those of pristine systems as outlined in Table 5.3 and Table 5.4. Bond lengths are essential in the understanding of the effect of various impurity levels on bonding mechanisms in compounds.

28

Table 5.3: calculated bond lengths (Å) before and after 2%,4%, and 6% doping of the two phases of TiO_2. Percentage deviations are given relative to calculated values of pristine TiO_2.

		Before	After	% Deviation
Bond lengths (Å)				
Anatase	**2%N**	Ti-O =1.96	Ti-O =1.93	-1.53
			Ti-N =1.95	-0.51
	4%N	Ti-O =1.96	Ti-O =1.94	-1.02
			Ti-N =1.94	-1.02
	6%N	Ti-O =1.96	Ti-O =1.95	-0.51
			Ti-N =1.93	-1.53
Rutile	**2% N**	Ti-O =1.96	Ti-O =1.94	-1.02
			Ti-N =1.96	-1.53
	4% N	Ti-O =1.96	Ti-O =1.96	-0.51
			Ti-N =1.94	-1.02
	6% N	Ti-O=1.96	Ti-O =1.95	-0.51
			Ti-N =1.93	-1.53

Table 5.3 suggest that Ti-O bond lengths in the anatase phase are reduced by 1.53% and 1.02% after 2% and 4% N doping, respectively. To examine the full impact of N doping on the symmetry of the pristine materials, the magnitude of Ti-N bond lengths was checked. It was interesting to note that on average, at 2% N doping, Ti-N bond lengths for N doped anatase and Ti-O bond lengths for pristine anatase are almost the same, but were reduced to 1.94 Å at 4% N doping and 1.93 Å at 6% N doping. This indicates that the replacement of N at O sites did not cause significant distortion in the lattice and therefore nitrogen is a good dopant structurally. For rutile, the percentage deviation of Ti-O bond lengths after doping versus before doping is about 1% at 2 % N and 4 % N doping, but less than 1% at 6 % N doping, implying that the rutile structure is also preserved after doping. The minor variations are attributed to the fact that, relative to oxygen, nitrogen has a smaller atomic radius. Nitrogen's atomic radius is 0.60 Å, while that of oxygen is 0.65 Å. Generally, the slight deviations on bond lengths shown in Table 5.3 shows that the substitution of N atom(s) at O site(s) creates very little strain on adjacent Ti atoms at 2% and 4% dopant concentrations. The structures are preserved after doping at 2% and 4% dopant concentrations, in both anatase and rutile cases. Table 5.4 compares estimated bond angles and bond lengths before and after doping.

Table 5.4: Calculated bond angles before and after 2%,4%, and 6% doping of TiO_2

		Before	After	% Deviation
Bond Angles (°)				
Anatase-	**2%N**	Ti-O-Ti =155.41	Ti-O-Ti =153.31	-1.4
			Ti-N-Ti=154.32	-0.7
	4%N	Ti-O-Ti =155.41	Ti-O-Ti =153.24	-0.6
			Ti-N-Ti= 153.09	-1.5
	6%N	Ti-O-Ti =155.41	Ti-O-Ti =150.44	+3.2
			Ti-N-Ti=150.44	+3.2
Rutile	**2% N**	Ti-O-Ti =131.94	Ti-O-Ti =130.81	-0.8
			Ti-N-Ti=131.16	-0.6
	4% N	Ti-O-Ti =131.94	Ti-O-Ti = 134.06	+2.2
			Ti-N-Ti= 135.13	+3.7
	6% N	Ti-O-Ti =131.94	Ti-O-Ti = 140.07	+6.4.
			Ti-N-Ti= 138.13	+5.8

The bond angles are reduced by 1.4% at 2% N and 0.6% when the TiO_2 anatase is doped with N, as shown in Table 5.4. However, 4% N doped rutile TiO_2 shows an increase in bond angles by 2.2% and 3.7%, respectively. Again, as stated earlier, this results from the difference in atomic radii of nitrogen and oxygen. However, some lattice stretch was observed at 6%N doping in both rutile and anatase TiO_2. In anatase, bond angles increased by 3.2% at 6%N doping, while in rutile TiO_2, bond angles increased by approximately 6%, making 4%N doping the best doping level in both rutile and anatase TiO_2.

5.2: Electronic Properties

The emphasis here is on band theory, which forms the basis for understanding all-solid-state devices and has also been used to define the physical properties of solids, (see section 3.2.2) which are important in identifying the relevant areas of application.

From the high symmetry points and paths created with XCrysDen (Kokalj and Causà, 2001), the band structure and projected density of state (Pdos) were computed.

5.2.1: Projected density of states and band structures for pristine and doped Rutile TiO₂

The band structures and Pdos for pristine and doped rutile TiO_2 at 2%, 4%, and 6% nitrogen concentrations are shown in figures 5.5 (a) - (d) and results discussed in this section.
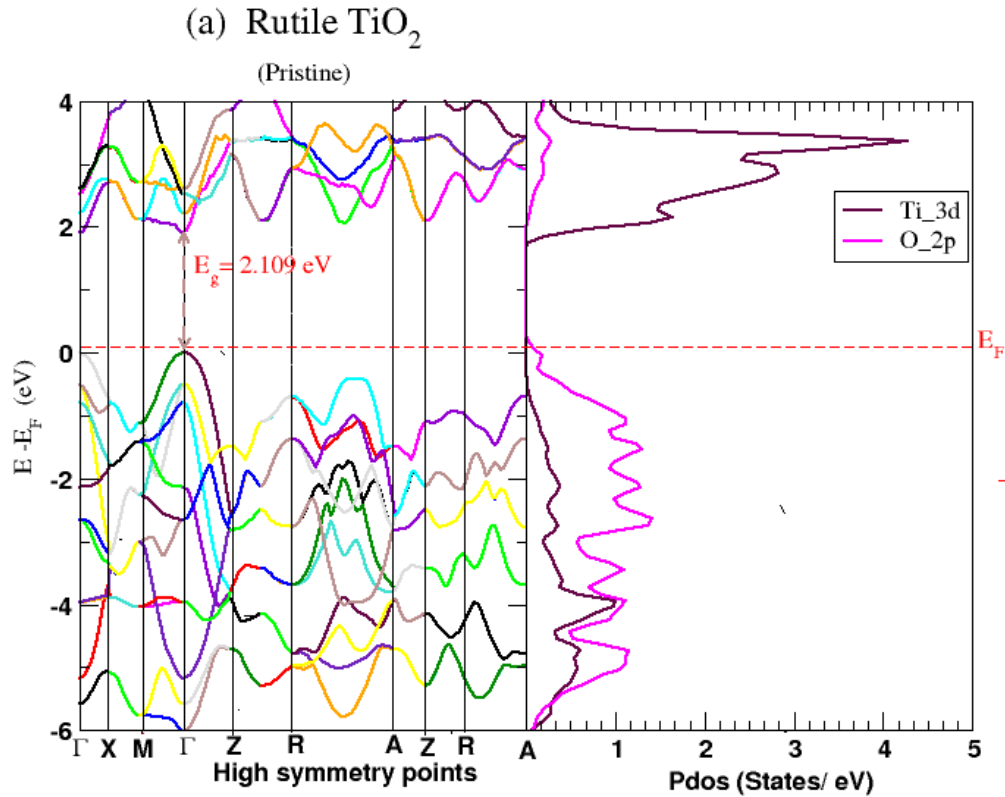
(a) Rutile TiO_2
(Pristine)
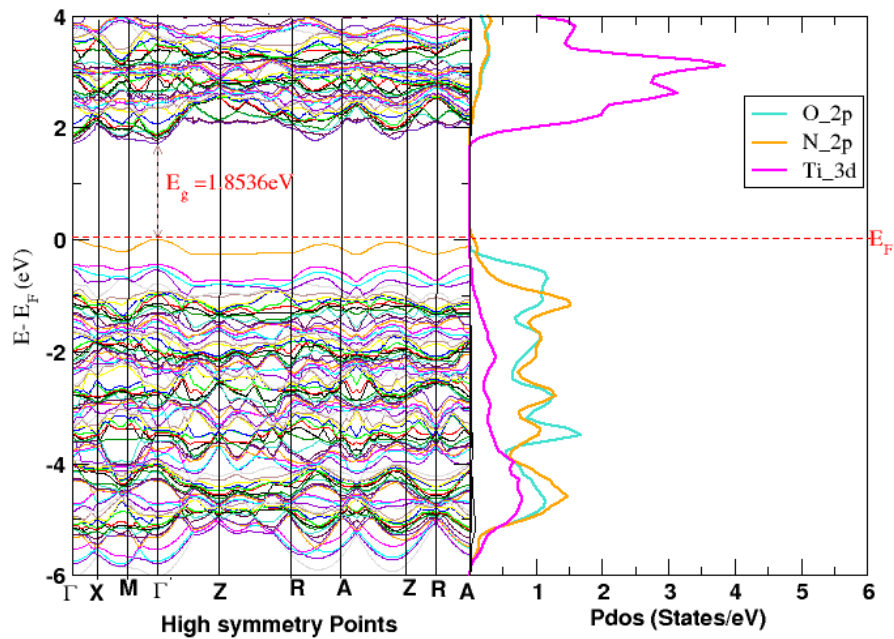
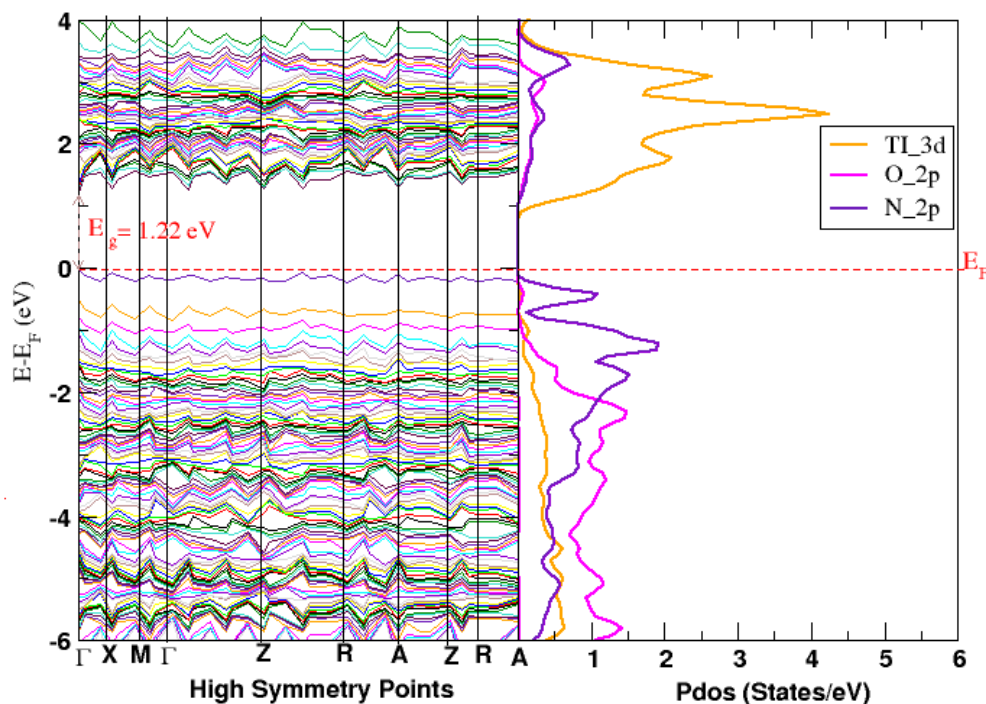(b) 2%N doped rutile TiO_2
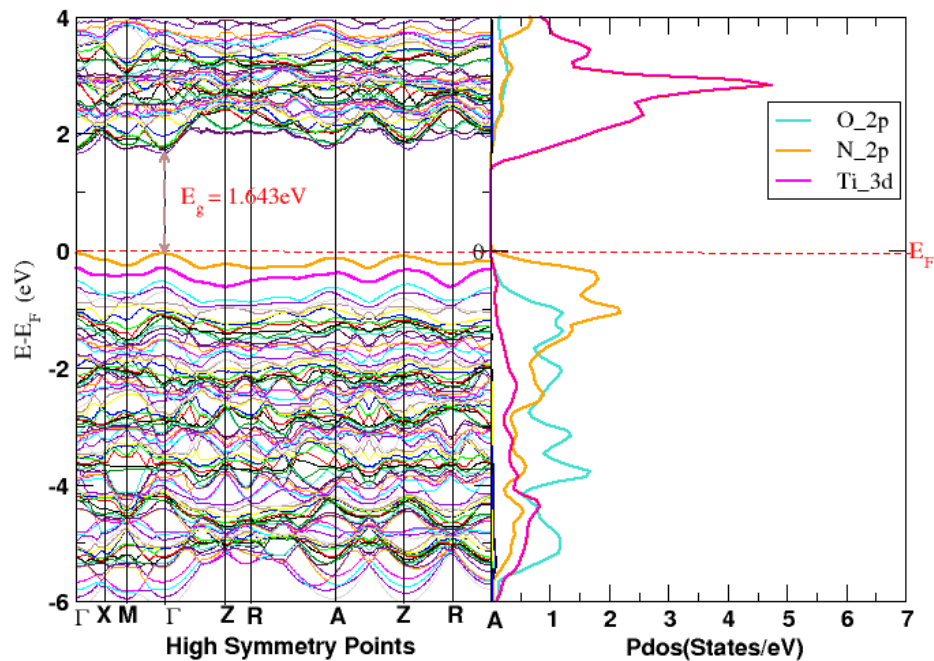
(c) 4%N doped rutile TiO_2

Figure 5.5: Band structure and Pdos for (a) pristine Rutile TiO_2 (b) 2% N doped Rutile TiO_2, (c) 4% N doped Rutile TiO_2 and (d) 6%N doped Rutile TiO_2.

In Figure 5.5 (a), 2.109 eV direct band gap of is found, with Ti 3d and O 2p orbitals as the band gap character. As seen in the Pdos plot, O 2p states dominates the valence band. The conduction band majorly comprises of Ti 3d states ranging from 2.1 eV to 4.0 eV. The additional bands between the VBM and CBM in Figure 5.5(b), (c), and (d) as a result of the contribution of N 2p states caused by nitrogen doping. Di Valentin *et al.* (2007) obtained similar results. For 2%, 4% and 6% doped rutile TiO_2, N 2p are situated at 0.25 eV, 0.47 eV, and 0.89 eV above VBM. This enhances visible light absorbance of TiO_2. According to Guo *et al.* (2011), these partially occupied states operate as a trap for excited electrons, thus lowering visible light absorbance of N doped rutile TiO_2. Looking closely at Figure 5.5(d), there is a major impact on the band structures of 6%N doping in rutile TiO_2. The shape of the bands is affected by this high dopant concentration. An upward shift of the Fermi level from 9.1745 eV to 9.4202 eV in rutile was noted for 2% N doping. At 4 % N doping, the Fermi level was raised to 9.6304 eV, while the band gap reduced to 1.643 eV. As a result of the N rutile doping, there was a reduction of band gap to 1.22 eV at 6%

N. The origin of this constant shift of Fermi towards the conduction band upon doping is an important note to be considered. The charge imbalance between N and the host lattice, as stated by Khan *et al*. (2013) for their Ag (Silver) doped anatase, contributes to this change in the Fermi level. The upward shift in the Fermi level means that it moved close to the conduction band, an indicator that the type of conductivity present is the donor type (Khan *et al*. , 2012; Matsumoto *et al.,* 2010). Di Valentin *et al*. (2007) and Khan *et al*. (2012) stated that substitution N doping results in N 2p impurities in TiO_2 band gap due to reduction of Ti^{4+} to Ti^{3+} in N doped TiO_2. Similarly, in this study, an introduction of oxygen vacancies to the system induces charge imbalance, Ti^{+4} is reduced to Ti^{+3} resulting in the redistribution of charge. Figure 5.6 shows the band structures and Pdos plots for pristine and N doped anatase TiO_2.

Figure 5.6 (a) shows that the VBM and CBM are on different high symmetry points indicating that anatase TiO_2 has an indirect band gap of 2.29 eV, from Z to Γ. In pristine anatase, more bands are observed than in pristine rutile, which arises from the fact that there are 6 atoms in rutile unit cell while there are 12 atoms in that of anatase. The Fermi level also shifts from 7.6143 eV to 8.094 eV upon 2% N doping, the gap decreases to 1.81 eV. A 4% N doping further shifts the Fermi level to 8.64 eV as well as a further change of the energy band gap to 1.644 eV, within DFT approximations. Further still, a band gap reduction to 1.075 eV is realized at 6%N doping in anatase. These findings are similar to those found in the rutile case and can also be related to the explanations for the above N doped rutile case. In comparison to the pristine anatase sample, the shape of the conduction band remains unchanged at 2 % N and 4 % N doping. The presence of N-2p impurity states, however, causes the shape of the valence band to be significantly altered.

5.2.2: Projected density of states and Band structures for pristine and doped Anatase TiO₂
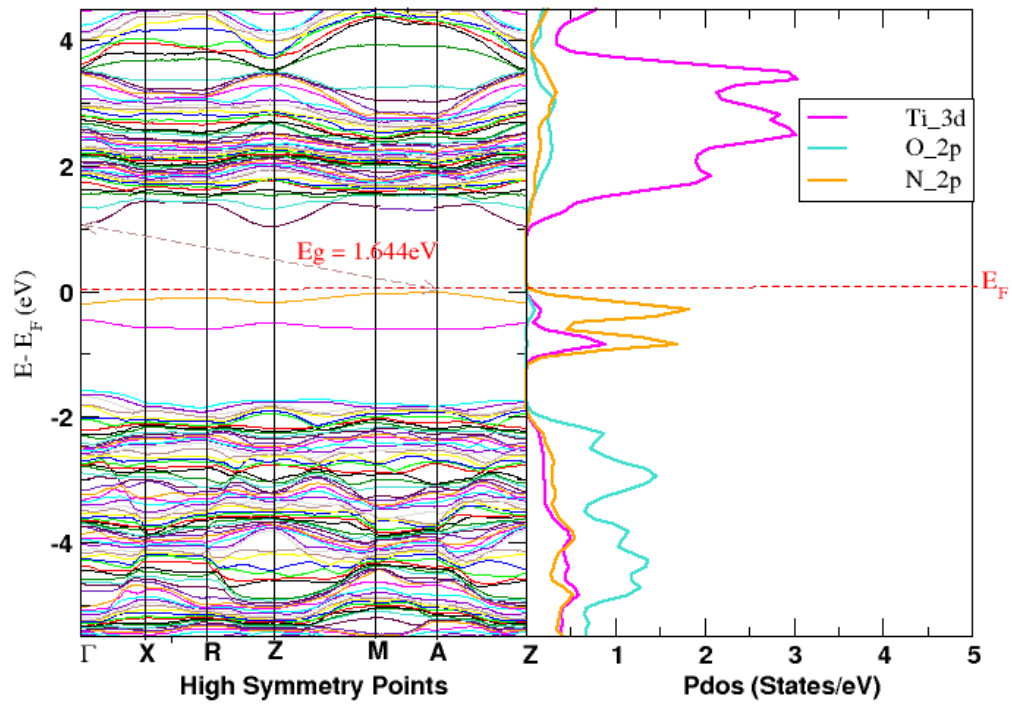
The band structures and Pdos for pristine and nitrogen doped anatase TiO₂ at 2%, 4% and 6% concentrations are shown in Figure 5.6 (a) - (d) followed by a comprehensive discussion of the results obtained.

(a) Anatase TiO₂
(Pristine)
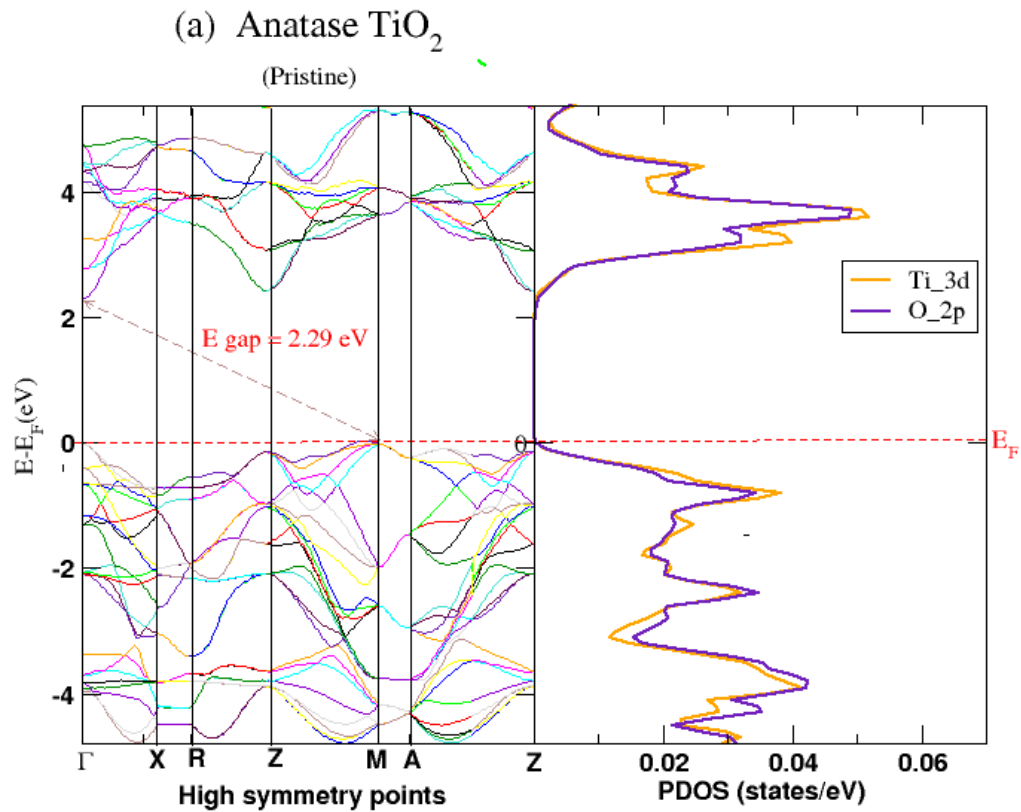
(b) 2%N doped anatase TiO$_2$
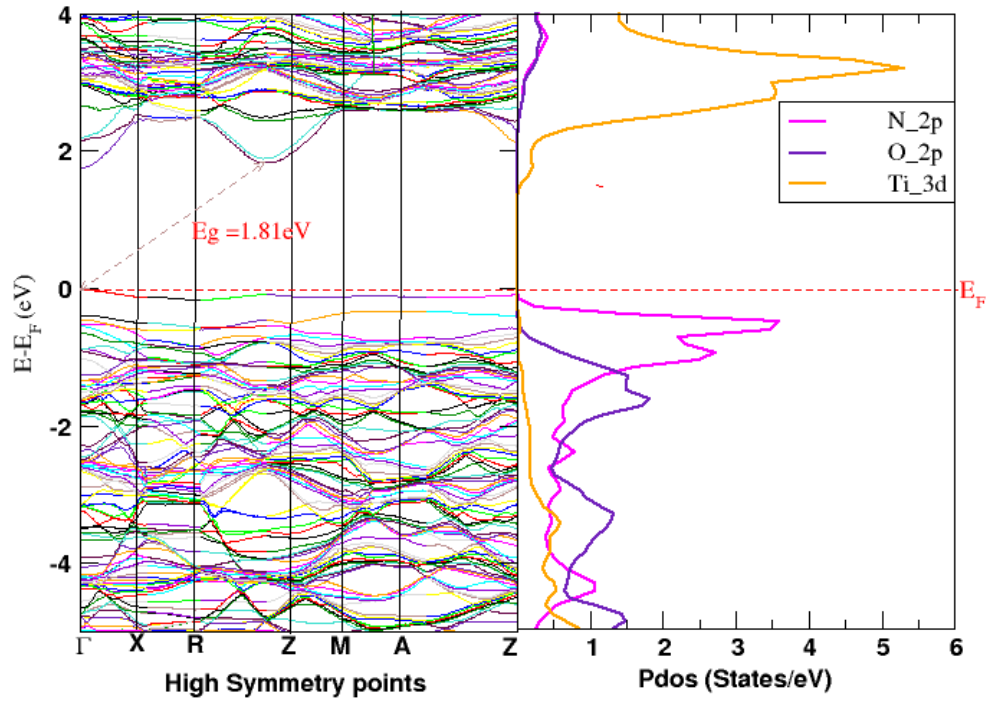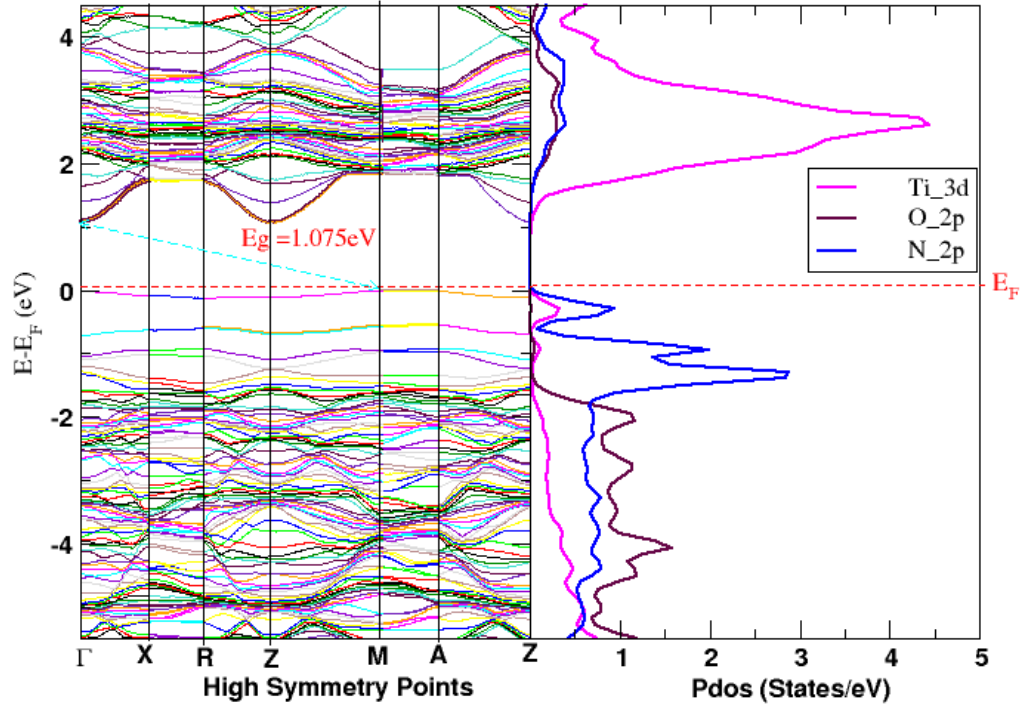

(c) 4%N doped anatase TiO$_2$

(d) 6%N doped anatase TiO$_2$

Figure 5.6: Band structure and Pdos for (a) pristine Anatase TiO$_2$ (b) 2% N doped Anatase TiO$_2$, (c) 4% N doped Anatase TiO$_2$ and (d) 6% N doped Anatase TiO$_2$.

The N-2p states are at about 0.48 eV, 0.65 eV and 0.98 eV above the VBM for 2%, 4% and 6% nitrogen-doped anatase TiO$_2$, respectively. N-2p states contributed to the band gap reduction in anatase TiO$_2$ upon 2% and 4% nitrogen doping, but still, the mid-gap states are formed. A closer look at Figure 5.6(d) shows that 6% N doping in TiO$_2$ anatase affects the shape of both valence and conduction bands, implying that TiO$_2$ anatase also has limits to which it can be doped. Nitrogen doping decreased the band gap of the pristine materials in both rutile and anatase TiO$_2$, but they both developed mid-gap states, with shallow energies, within the band gaps. In solar energy applications, these mid-gap states are known to lower the absorption threshold. According to Stengl and Bakardji *et al.* (2010), The mid-gap states act as traps for photo-generated carriers, reducing photo-generated current and, as a result, limiting the photo-activity of N doped TiO$_2$.

For further investigations of the behavior of charges before and after doping, charge density calculations for pristine and doped structures were performed and analyzed in Figure 5.7.
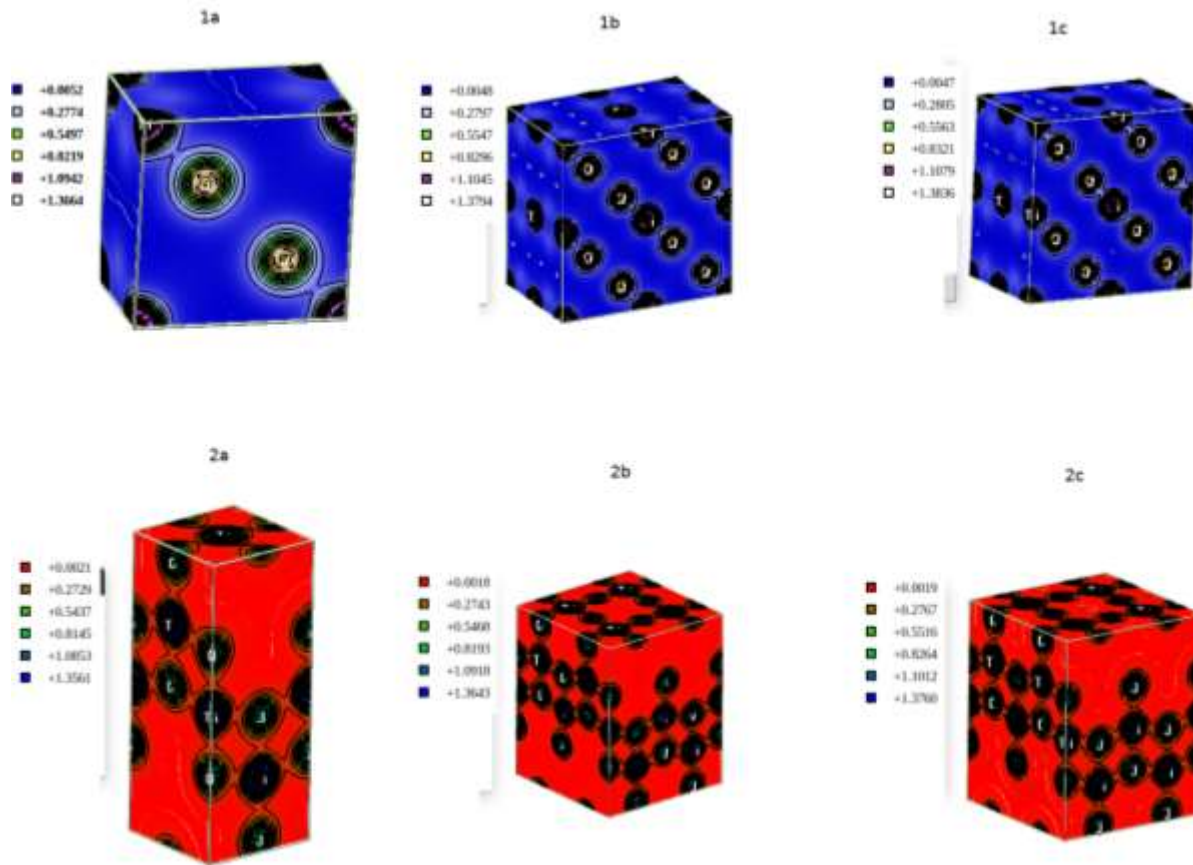
Figure 5.7: The charge distribution in (1a) Pristine rutile TiO_2, (1b) 2% N doped rutileTiO_2 supercell, and (1c) 4% N doped rutile TiO_2 supercell, while Figure (2a), (2b), (2c) represent the charge density distributions for Pristine anatase TiO_2, 2% N doped anatase TiO_2 supercell, and 4% N doped anatase TiO_2 supercell, respectively.

We often talk of the density of the charge when defining the volume of charge in continuous charge distribution. Charge density tells how much charge a particular area of space occupies at any point in space, and provides valuable knowledge about bonding in various structures (Lang *et al.,* 1970). The calculated distribution of charge density in TiO_2 polymorphs is shown in Figure 5.7, with thermometer scales showing electric charge density per unit volume/area in arbitrary units, indicating where the charge is likely to be spatially concentrated.

The charge distributions in the atoms are not uniform. As depicted in Figure 5.7, the tightly held valence states have higher charge density, and the converse is true as we move away from the inner states. Owing to the minimum interference between the atoms, low-density charge distributions are visible on the 3D planes around them. For both compositions, the three-dimensional maps show

the prevailing ionic nature between Ti, O, and N, the charges density is more concentrated near the Ti atoms, and this increases with an increase in dopant concentration. This illustrates the fact that the number of cation vacancies increases with increased doping concentration on the TiO_2 host lattice, as suggested by Mangaiyarkkarasi *et al*. (2016).
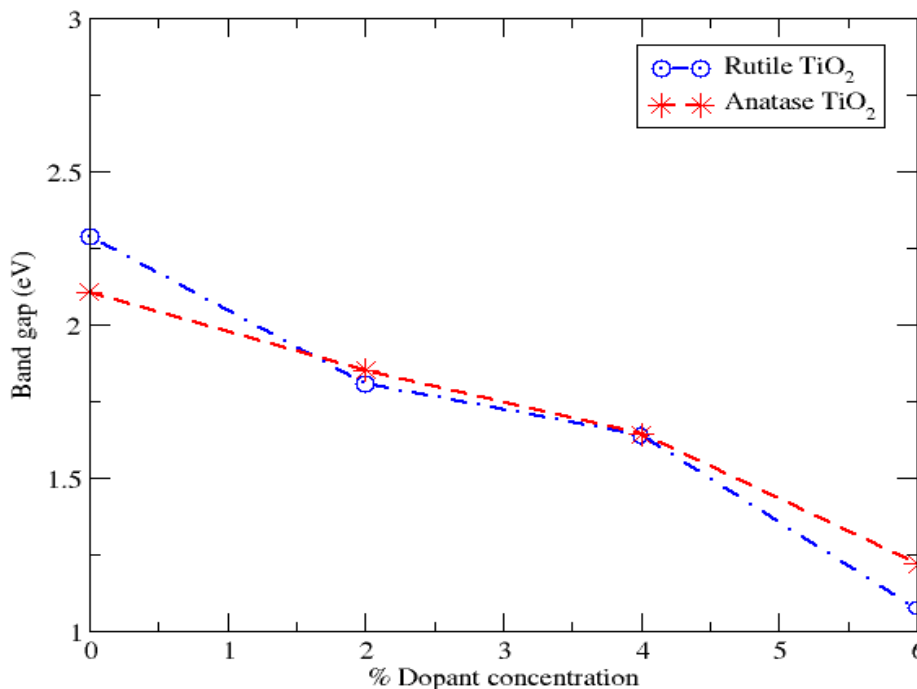

Figure 5.8: A plot of the band gap with increasing dopant concentration.

Figure 5.8 indicates that the band gap is reduced as dopant concentration is increased in both nitrogen-doped rutile and anatase TiO_2. As stated earlier in chapter one of this study, TiO_2 band gap should be reduced to improved photo-activity. This has been achieved in N-doped TiO_2, but mid-gap states were created. Therefore, we had to take a look at both corundum Ti_2O_3 and the oxynitride Ti_2N_2O.

5.3: Band structure and Pdos for Corundum Ti_2O_3.

Corundum Ti_2O_3, a parent phase of Ti_2N_2O structures, appeared metallic, being consistent with other DFT findings (Aoki *et al.,*2019). In the whole band structure, the dominating states are Ti-3d and O-2p (see Figure 5.9). Samat *et al.* (2019) discovered that corundum Ti_2O_3 has a small band gap of 1.65 eV, which DFT simulations failed to predict correctly. In most systems, DFT is known to underestimate band gaps.
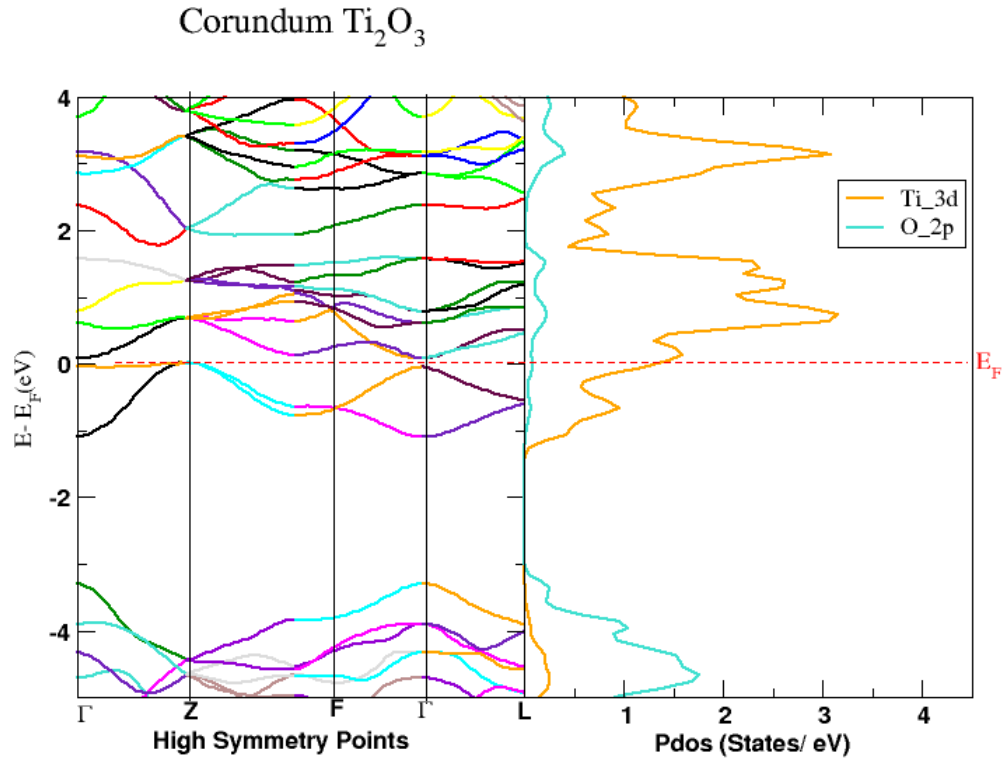
5.9 Band structure and Pdos for Corundum Ti_2O_3.

To account for the localization of the titanium 3d orbitals, so as to achieve a more accurate electronic band gap, a moderated Hubbard potential, U, was added to electronic structure calculations. The technique for optimizing the U correction can be defined from fundamental principles or carried out empirically by varying the U value and comparing it to the experimental results of the properties of the systems. The latter was implemented in this study. The choice of U was made following a series of calculations with various Coulomb interaction parameters, U of the order of 1 eV to 7 eV. The impact of different values of U on the bandgaps of the oxides was recorded in Table 5.5 and Figure 5.10.

Table 5.5: Optimization of the U values for TiO_2 (anatase and rutile) and Ti_2O_3

Values of U (eV)	Band gap (eV) This work.		
	Anatase TiO_2	Rutile TiO_2	Corundum Ti_2O_3
1	2.61	2.09	0.11
2	2.86	2.32	0.49
3	**3.01**	2.56	0.87
4	3.36	2.62	1.36
5	3.61	**2.70**	**1.63**
6	3.86	3.47	1.76
7	4.12	3.61	1.86
Experimental	3.2[a]	3.0[a]	1.65[b]

[a]Yang *et al.* (2010) [b] Li *et al. (*2018)

The best estimation of the band gap (**bold**) when seeking agreement with experimental findings from Yang *et al.* (2010) and Li *et al.* (2018) was realized at U = 3 eV, 5 eV and 5 eV, respectively, for anatase TiO_2, rutile TiO_2, and Corundum Ti_2O_3. The band gaps increased with increasing values of U, as indicated in Figure 5.9
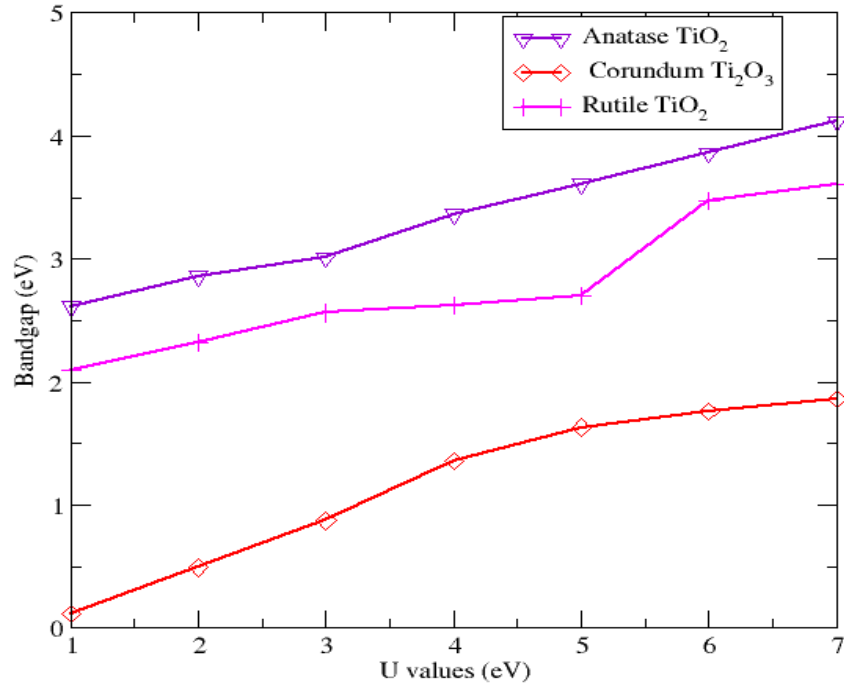
Figure 5.10: A plot of band gap versus *U* values for anatase, rutile, and corundum structures.

DFT+U gave predictions closer to the gaps presented in experiments. In DFT+U studies, Corundum Ti_2O_3, which showed metal-like properties, opened up a small band gap of 1.64 eV, indicating semiconducting properties. As shown in Table 5.6, these corrections are in good keeping with experimental findings. Figure 5.11 (a) (b), and (c) shows the corrected band structures for anatase TiO_2, rutile TiO_2, and corundum Ti_2O_3.
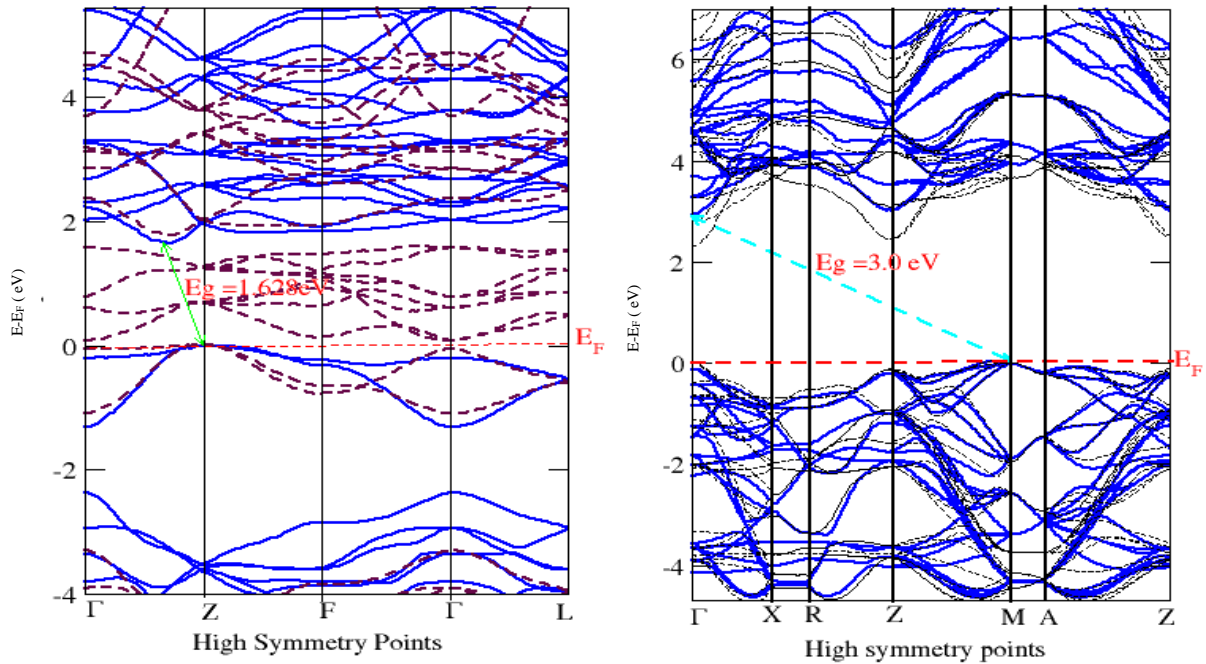
(a)

(b)
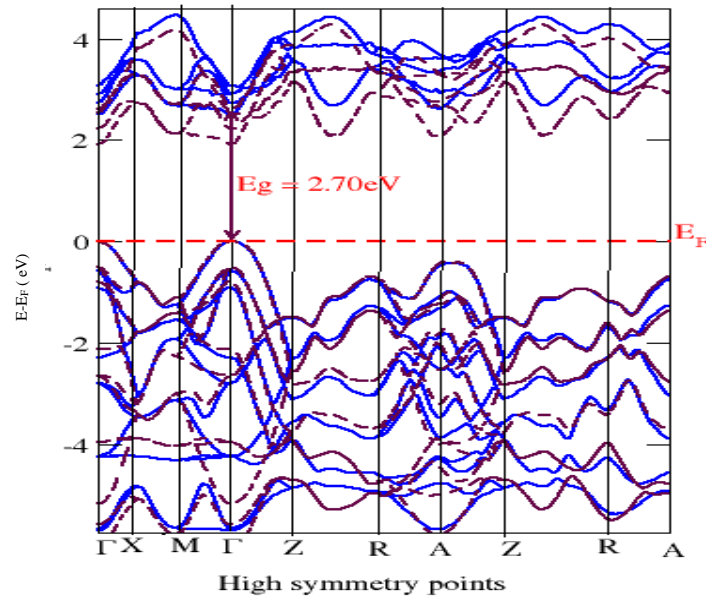
(c)

Figure 5.11: (a)-(c) superimposed band structures for plain DFT and DFT+U, (a) CorundumTi$_2$O$_3$, (b) Anatase, and (c) Rutile, black dotted are calculated by DFT-GGA while the blue solid is the DFT+U calculated bands.

It is also important to examine the impact of U on the lattice parameters. Table 5.6 summarizes the obtained lattice parameters in regard to Hubbard values.

Table 5.6: Calculated lattice parameters in variation with the Hubbard values.

Value of U	Lattice parameters					
	This work					
	Anatase TiO_2		Rutile TiO_2		Corundum Ti_2O_3	
	a (Å)	c/a	a (Å)	c/a	a (Å)	c/a
1	3.85	2.52	4.62	0.65	5.22	1.01
2	3.86	2.53	4.63	0.64	5.24	1.02
3	3.80	2.52	4.64	0.65	5.25	1.03
4	3.82	2.54	4.65	0.64	5.19	1.01
5	3.83	2.57	4.63	0.63	5.16	1.00
6	3.92	2.58	4.66	0.65	5.38	1.00
7	4.05	2.59	4.67	0.66	5.35	1.03
Experimental	3.78	2.57	4.64	0.65	5.15	1.01

From Table 5.6, it is observed that at the   optimized U values, the lattice parameters 'a' for the three oxides were 3.80 Å at U= 3 eV for anatase TiO_2, 4.63 Å at U = 5 eV for rutile TiO_2, and 5.16 Å at U = 5 eV for Ti_2O_3. These agree well with the   optimized lattice parameters at U=0 of this study, indicating that the lattice geometry was preserved. These findings are agrees well with those of Yang *et al.* (2010) and Li *et al.* (2018). German *et al.* 2017, when balancing geometric changes and electronic properties of TiO_2, reported optimum values of lattice parameter 'a' as 3.80 Å at U = 3 eV for anatase and 4.61 Å for rutile at U = 5 eV, which are in good agreement with this study.

5.4: Titanium Oxynitrides (Ti_2N_2O)

An alternative way of constructing Ti-N-O compounds is nitrogen doping into Ti_nO_{2n-1} phases. For example, a series of Ti_2N_2O oxynitrides can be developed when two of the 2n-1 oxygen atoms in Ti_nO_{2n-1} compounds with nitrogen. The corundum Ti_2O_3 primitive unit cell has two formula units comprising a total of four Ti and six O atoms (see Figure 5.1(c)). Substituting four out of six oxygen atoms with nitrogen to construct the Ti_2N_2O compound results in two Ti_2N_2O formula units in a unit cell (Aoki *et al.,*2019). There are 15 alternatives for nitrogen-substitution. However, only three forms were considered due to the nature of the pristine material. We called them P1, P2, and P3. The atomic positions were fully relaxed and cell parameters are optimized.
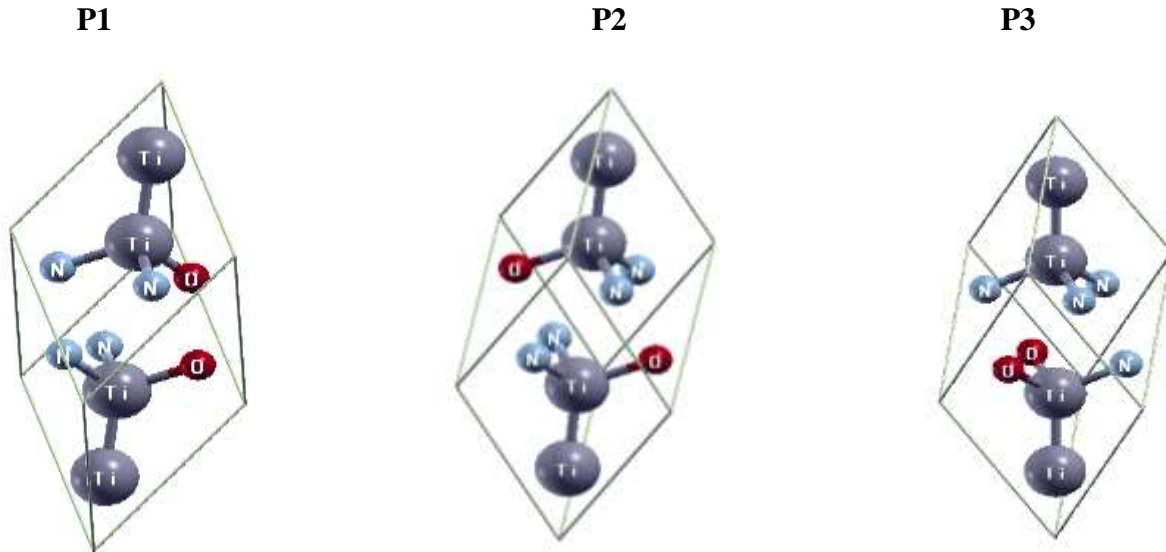

Figure 5.12: Different orientations of Nitrogen substitutions in Ti_2O_3 structure. P2 has an inversion symmetry while P1 and P3 do not have.

The oxynitrides were also modeled using the hexagonal convectional cell of Ti_2O_3 containing twelve titanium and eight oxygen atoms (Aoki *et al.,* 2019). This was viewed in XCrysDen at four different angles of projection as shown in Figure 5.12.
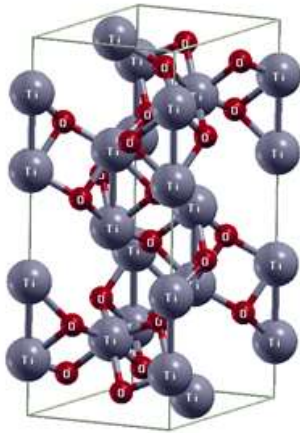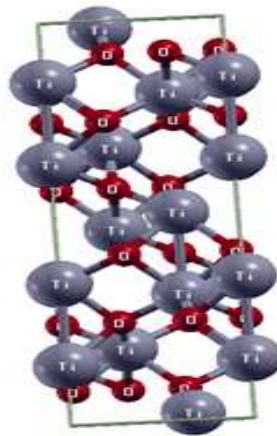
(a) Birds eye view.

(b) Projection in the direction of a + b

(b) Top view

d) projection in the direction of b

Figure 5.13: Four different angles of projection of Ti_2O_3 convectional unit cell, large purple balls, and Ti and O atoms are symbolized by small red balls.

Twelve out eighteen oxygen atoms were replaced by nitrogen in seven different ways to form the seven samples of the oxynitrides (S1 to S7), projected in the direction of a+b (for a clearer view) as shown in Figure 5.13. Ti_2N_2O-S structures are the samples of N doped hexagonal convectional cell of Ti_2O_3 at various O substitutional sites.
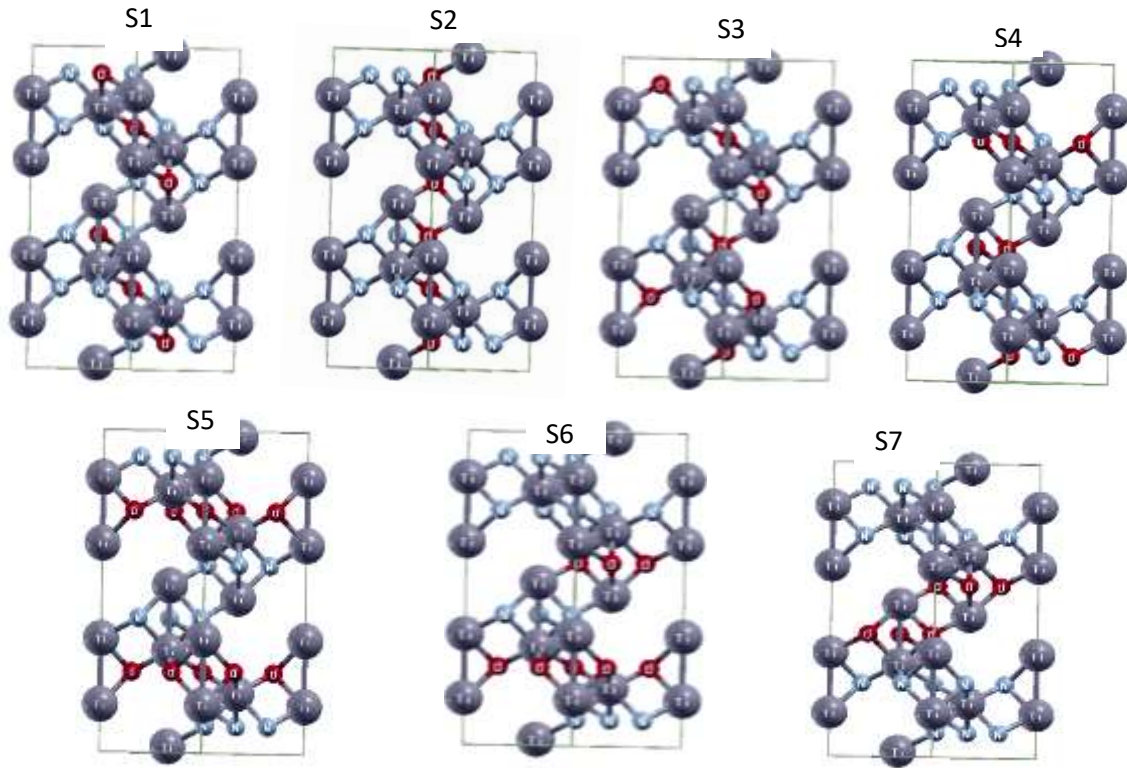

Figure 5.14: Side views of seven modeled titanium oxynitrides (Ti_2N_2O) projected in the direction of a+b, Ti, O, and N atoms are indicated by large purple balls, small red balls, and small blue balls, respectively.

Atomic positions were fully relaxed and cell parameters were optimized. The stability of the Ti_2N_2O-P structures was compared in Figure 5.15(a). The Ti_2N_2O-P structures are the samples of N doped primitive cells of Ti_2O_3 at different O substitutional sites. The plots indicate that P1 has the lowest energy, thus the most stable. In Figure 5.15(b), the same comparison was made for the S structures (S1to S7). The S1 has the lowest energy hence the most stable among the S structures.
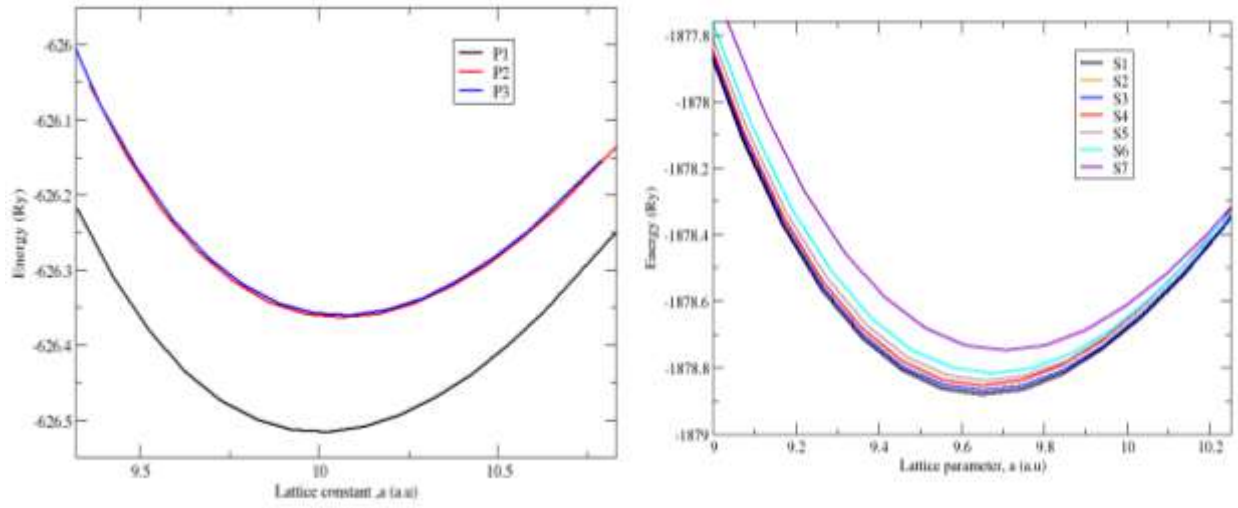
(a)

(b)
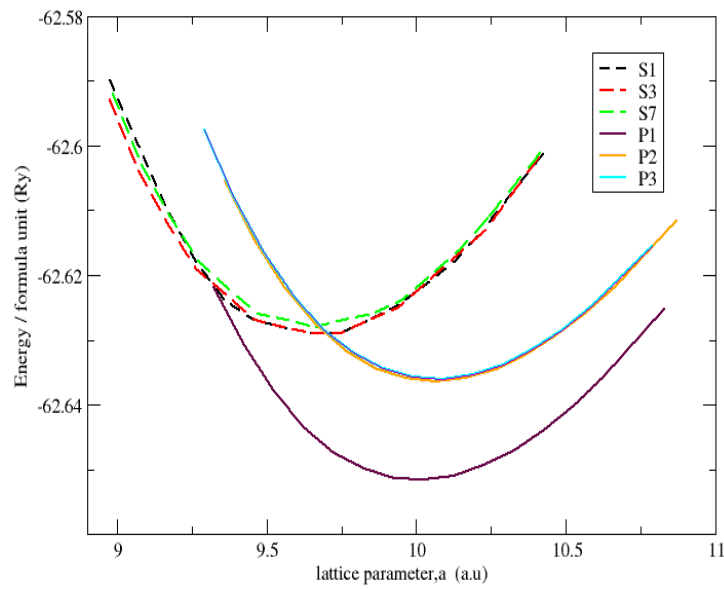
(c)

Figure 5.15: Energies versus lattice parameters of (**a**) the three orientations of nitrogen substitution into Ti_2O_3 structure (P-samples), and (**b**) seven different orientations of nitrogen substitution into Ti_2O_3 hexagonal convectional cell (S-samples), while (**c**) is the energy per formula unit for both P and S- structures of nitrogen substitution into Ti_2O_3 primitive and hexagonal convectional cells.

As indicated in Figure 5.15(b), the stability of the rest of the S structures lie within those of S1-S7, hence, S1, S3 and S7 were considered on Figure 5.15(c), which indicates that of all structures, P-structures are more stable than S-structures, with P1 being the most stable. This agrees well with the results of Aoki *et al.* (2019), where GW studies were employed on the oxynitrides. Therefore, in Figure 5.16, P-structures were considered for further analysis of their band structure, energy gap, and projected state density (Pdos).
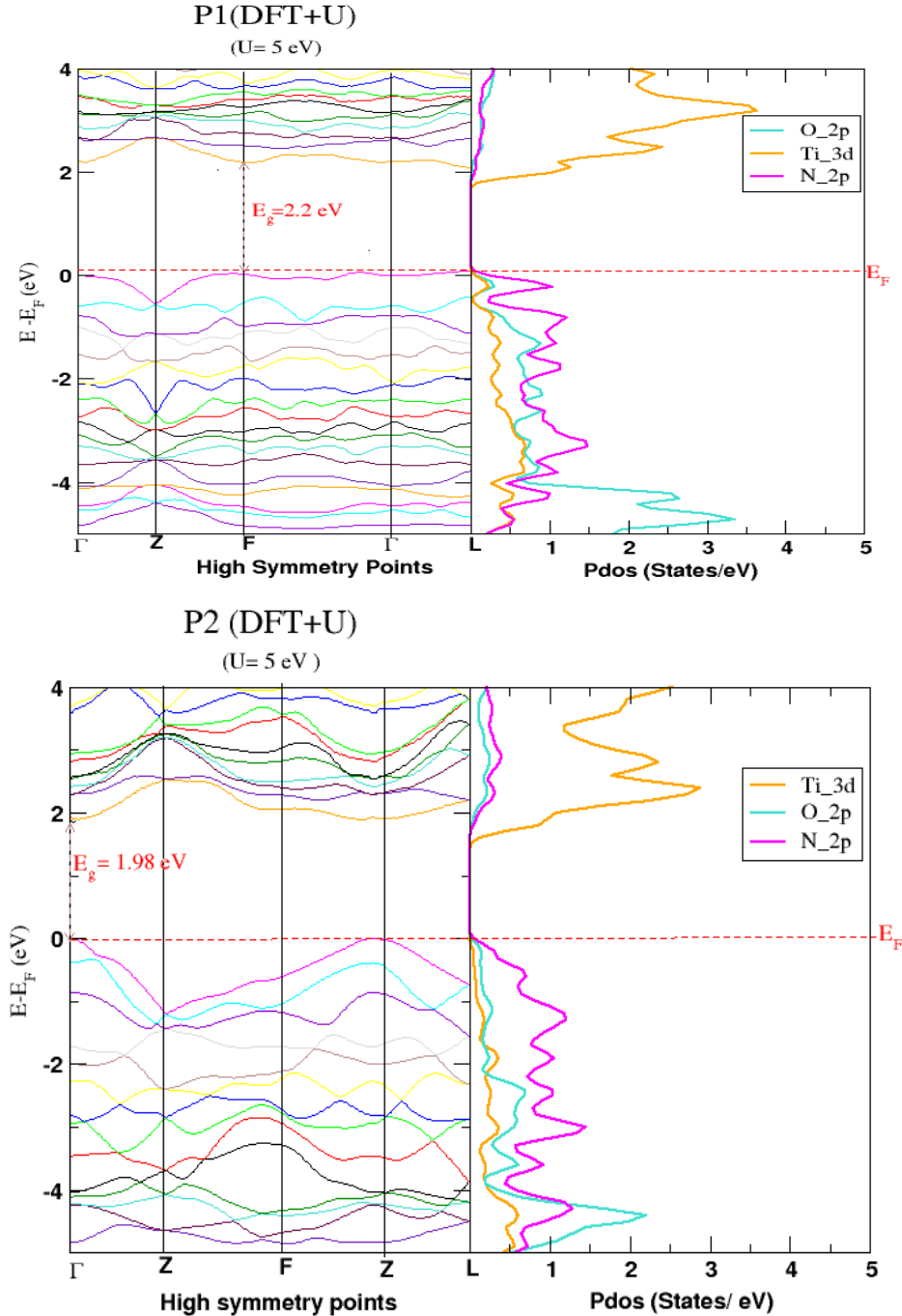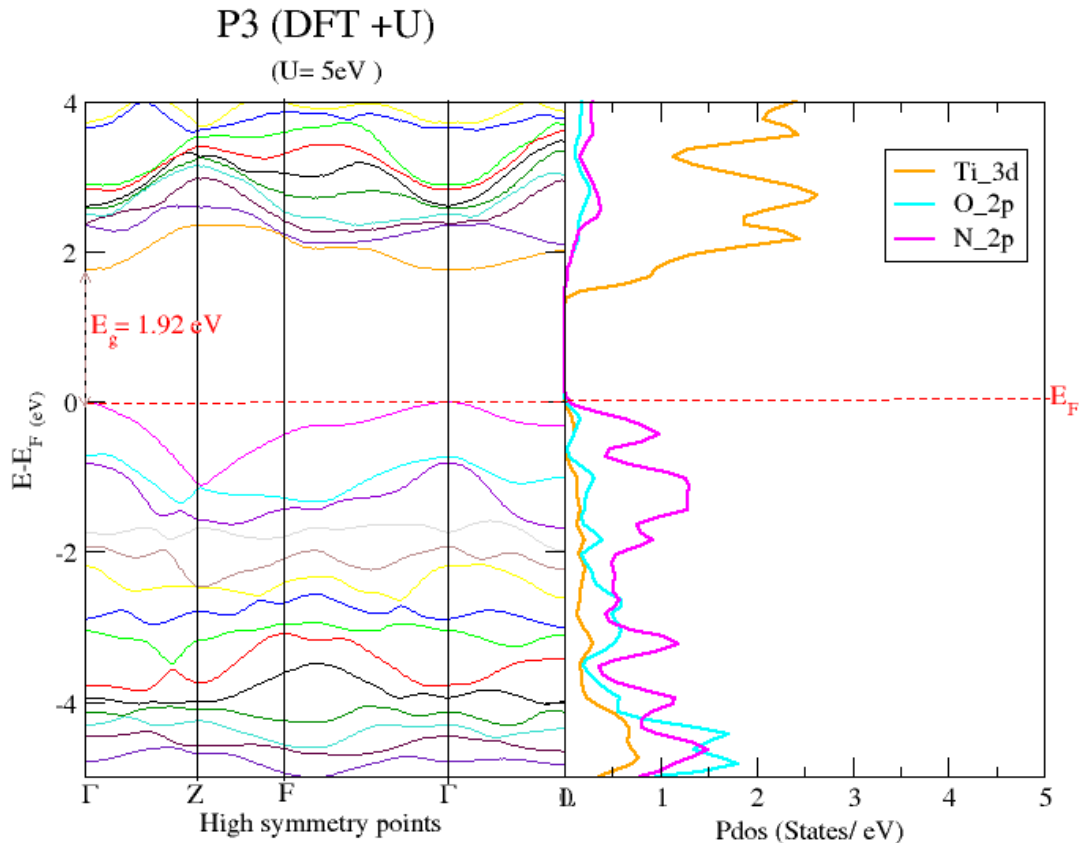
Figure 5.16: Band structures and Pdos for Corundum-based Ti_2N_2O P-Structures, (a) P1, (b) P2, and (c) P3, using DFT+U (U=5 eV) method.

The substitution of nitrogen into Corundum Ti_2O_3 opened up a gap of 1.33 eV within DFT approximations that translated to 2.2 eV via DFT+U studies with U= 5 eV, in the most stable sample, P1. The P2 and P3 samples had 1.98 eV and 1.92 eV band gaps, respectively. In all the three (P1, P2, and P3) samples, a band gap character of Ti 3d / N 2p orbitals were observed. Some hybridization between N-2p and Ti-3d states was also observed in the valence band.

Contrary to the case in N: TiO_2, no mid-gap states were formed within the intrinsic gaps of Ti_2O_3 after N substitution, therefore the absorption threshold is not affected.

We have successfully reduced the band gap of TiO_2 to improve its photo-activity without necessarily forming the mid-gap states that are known to serve as recombination centers for photo-excited electrons. Compared to pristine TiO_2, Ti_2O_3, and N: TiO_2, this study indicates that Ti_2N_2O structures are more promising photo-catalytic / photo-voltaic materials.

Table 5.7 gives a summary of the obtained band gaps as compared to experimental band gaps of the structures.

Table 5.7: Summary of the calculated and experimental band gap for the structures.

MATERIAL	ENERGY BAND GAP (eV)			
	THIS WORK (GGA)	THEORETICAL (GGA)	THIS WORK (DFT+U)	EXPERIMEN TAL
Anatase TiO_2	2.29	2.28[a]	3.0 (U=3 eV)	3.2 [c]
Rutile TiO_2	2.11	1.89[a]	2.7 (U=5 eV)	3.0 [c]
Corundum Ti_2O_3	No gap	No gap[b]	1.638 (U=5 eV)	1.65[d]
Oxynitrides Ti_2N_2O (P1) Ti_2N_2O (P2) Ti_2N_2O (P3)			2.20 (U=5 eV) 1.98 (U=5 eV) 1.92 (U=5 eV)	

[b]Aoki *et al.* (2019) [a] Samat *et al.* (2019) [c]Yang *et al.* (2010) [d] Li *et al. (*2018)

As described in the preceding sections of this chapter, the DFT+U gave predictions closer to the gaps presented in experiments. The summarized results on Table 5.7 is a clear indication that the oxynitrides are more promising materials for solar energy applications. These results are well comparable with the experimental findings by Yang *et al.* (2010).   Li *et al. (*2018) reported experimental gap of 1.65 eV for corundum Ti_2O_3.

CHAPTER 6: CONCLUSION AND RECOMMENDATIONS

6.1 CONCLUSION

The structural and electronic properties of pristine and doped tetragonal TiO_2 (anatase and rutile), corundum Ti_2O_3, and oxynitride Ti_2N_2O have been studied in this work. The lattice parameters obtained from DFT calculations, reproduced quite well the experimental data even though these calculations assume defect-free structures.

This study showed that the inclusion of nitrogen in the matrix of either anatase or rutile TiO_2 did not substantially affect structural properties, with bond lengths varying in both cases by slightly more than 1%, which resulted from the difference in atomic radii of O and N causing little strain to the adjacent Ti atoms.

On doped band structures, the Fermi level moved towards the conduction band as a result of the n-type doping. Rutile TiO_2 band gap of 2.11 eV was reduced to 1.85 eV, 1.64 eV, 1.22 eV, on 2% N, 4% N, and 6% N doping, respectively, while in anatase the band gap of 2.29 eV, reduced to 1.81 eV, 1.64 eV, and 1.07 eV on 2% N, 4% N, and 6% N doping, respectively.

There was a shift of the band gap character from Ti-3d / O-2p orbitals to Ti-3d / N-2p orbitals upon doping. Mid-gap states were observed in doped band structure owing to the presence of N-2p impurity states, which function as traps for excited electrons, reducing the materials' efficiency.

The best doping level for both N doped rutile and anatase TiO_2 at substitutional sites is 4%.

The band gaps of N: TiO_2 reduced as the dopant concentration was increased up to 4%, beyond which the band structure appeared distorted. TiO_2 was therefore found to have limits to which it can be doped suggesting investigations of the oxygen-deficient corundum Ti_2O_3 which displayed metal-like properties within DFT approximations but opened up a band gap of 1.638 eV by DFT+U (U=5 eV) studies which was found to be consistent with experimental data.

By partial substitution of nitrogen in both primitive and hexagonal convectional cells of the parent Ti_2O_{2n-1} (n=2) structures, a variety of titanium oxynitride $Ti_nN_2O_{2n-3}$ (n=2) were modelled and analyzed in this study. The most stable sample (P1) of the oxynitride (Ti_2N_2O) had a band gap of 2.2 eV and did not have mid-gap states. For these reasons, Ti_2N_2O is a better photocatalytic material as the band gap obtained is close to the middle of the visible light region of the electromagnetic spectrum relative to TiO_2, N: TiO_2, and Ti_2O_3 materials.

6.2 RECOMMENDATIONS FOR FURTHER WORK

While considering the electronic structure calculations of Ti-based oxides with an aim of achieving more precise predictions, it is necessary to explore more intensive theories that employ many body approaches as used in the Yambo code (Marini *et al.,* 2009: Atambo *et al.,* 2019).

Ti-based oxides in the form of Ti_2O_{2n-1}, n≥2 may have other possible applications in addition to their applications as photo-catalysts and photovoltaic materials. Ti_2O_3 has a low transmittance but a high reflectance in the near-IR region, suggesting that it could be used as a temperature monitoring coating (Sedghi-Ghamchi *et al.,* 2007). This field is currently developing because little is known about the dielectric characteristics and optical band gap energy of Titania's higher oxide phases, among other aspects. Electronic and structural properties of Ti_2O_{2n-1}, n≥2, doped with other non-metals also be interesting to investigate.

This research provides a systematic way of obtaining a variety of titanium oxynitride compounds $Ti_nN_2O_{2n-3}$, with a detailed analysis of the n=2 cases. It is recommended that this approach would be extended to other transition-metal oxynitrides.

REFERENCES

Aoki, Y., Sakurai, M., Coh, S., Chelikowsky, J. R., Louie, S. G., Cohen, M. L., and Saito, S. (2019). Insulating titanium oxynitride for visible light photocatalysis. *Physical Review B*, *99***(7)**, 075203-075206.

Belogolova, E. F., and Sidorkin, V. F. (2004). Ab initio and DFT study of the structure of pentacoordinated silicon compounds: Si-substituted (O–Si) dimethyl (N-acetylacetamidomethyl) silanes. *Journal of Molecular Structure: THEOCHEM*, *668***(2–3),** 139–145.

Burke, K. (2007). The abc of dft. *Department of Chemistry, University of California press*, 40-41.

Chen, X., Liu, L., Peter, Y. Y., and Mao, S. S. (2011). Increasing solar absorption for photocatalysis with black hydrogenated titanium dioxide nanocrystals. *Science*, *331***(6018),** 746–750.

Chen, X., and Selloni, A. (2014). Introduction: Titanium dioxide (TiO_2) nanomaterials. *Chemical Reviews*, *114***(19)**, 9281–9282.

Chakraborty, P. (2009). Introducing: The Photonics Society of India. *Physical Review B*, *791***(2),** 20-25

Di Valentin, C., Finazzi, E., Pacchioni, G., Selloni, A., Livraghi, S., Paganini, M. C., and Giamello, E. (2007). N-doped TiO_2: Theory and experiment. *Chemical Physics*, *339***(1–3)**, 44–56.

Dorado, B., Amadon, B., Freyss, M., and Bertolus, M. (2009). DFT+ U calculations of the ground state and metastable states of uranium dioxide. *Physical Review B*, *79***(23),** 205-225

Donev, A., Nonaka, A., Bhattacharjee, A. K., Garcia, A. L., and Bell, J. B. (2015). Low Mach number fluctuating hydrodynamics of multispecies liquid mixtures. *Physics of Fluids*, *27***(3)**, 037103-037105.

Etacheri, V., Di Valentin, C., Schneider, J., Bahnemann, D., and Pillai, S. C. (2015). Visible-light activation of TiO_2 photocatalysts: Advances in theory and experiments. *Journal of Photochemistry and Photobiology C: Photochemistry Reviews*, *25***,** 1–29.

Filippone, F., Mattioli, G., Alippi, P., and Bonapasta, A. A. (2009). Properties of hydrogen and hydrogen–vacancy complexes in the rutile phase of titanium dioxide. *Physical Review B*, *80***(24)**, 245203-245206.

Foundation, I. association with T. W. (2014). *Titanium Dioxide Photocatalysis: A New Kind of Water Treatment*. RSC Education. October 30, 2019 review, *34***,** 26–28.

Fujishima, A., Zhang, X., and Tryk, D. A. (2008). TiO_2 photocatalysis and related surface phenomena. *Surface Science Reports*, *63***(12)**, 515–582.

German, E., Faccio, R., and Mombrú, A. W. (2017). A DFT + *U* study on structural, electronic, vibrational and thermodynamic properties of TiO_2 polymorphs and hydrogen titanate: Tuning the Hubbard ' *U* -term.' *Journal of Physics Communications*, *1***(5)**, 055006-055009.

Giannozzi, P., Baroni, S., Bonini, N., Calandra, M., Car, R., Cavazzoni, C., Ceresoli, D., Chiarotti, G. L., Cococcioni, M., and Dabo, I. (2009). QUANTUM ESPRESSO: A modular and open-source software project for quantum simulations of materials. *Journal of Physics: Condensed Matter*, *21***(39)**, 395502-39506.

Giustino, F. (2014). *Materials modelling using density functional theory: Properties and predictions*. Oxford University Press, 101–129.

Goh, E. S., Mah, J. W., and Yoon, T. L. (2017). Effects of Hubbard term correction on the structural parameters and electronic properties of wurtzite ZnO. *Computational Materials Science*, *138***(2-3)**, 111–116.

Harrison, W. A. (2004). *Elementary Electronic Structure: Revised*. World Scientific Publishing Company.

Hendrik, J. (1976). Monkhorst, and James D. Pack. *Phys. Rev. B*, *13*, 5188-5231.

Hu, Z., and Metiu, H. (2011). Choice of U for DFT+ U calculations for titanium oxides. *The Journal of Physical Chemistry C*, *115***(13)**, 5841–5845.

Jensen, S., and Kilin, D. (2012). Anatase (100) thin film surface computational model for photoelectrochemical cell. *International Journal of Quantum Chemistry*, *112***(24),** 3874–3878.

Khan, M., Xu, J., Chen, N., Cao, W., Usman, Z., and Khan, D. F. (2013). Effect of Ag doping concentration on the electronic and optical properties of anatase TiO_2: A DFT-based theoretical study. *Research on Chemical Intermediates*, *39***(4),** 1633–1644.

Kohn, W., and Sham, L. J. (1965). Self-consistent equations including exchange and correlation effects. *Physical Review*, *140***(4A)**, A1133-A1135.

Kokalj, A., and Causà, M. (2001). *XCrySDen:(X-Window) CRYstalline Structures and DENsities, 40(2), 13–14.*

Kroll, P. (2005). A DFT study of amorphous silicon oxynitride. *Journal of Non-Crystalline Solids*, *351***(12–13),** 1127–1132.

Lazzeri, M., Vittadini, A., and Selloni, A. (2001). Structure and energetics of stoichiometric TiO_2 anatase surfaces. *Physical Review B*, *63***(15)**, 155409-155412.

Lykos, P., and Pratt, G. W. (1963). Discussion on the Hartree-Fock approximation. *Reviews of Modern Physics*, *35***(3)**, 496-500.

Mahendra, I. P., Huda, A., Ngoc, H. M., Nghia, P. T., Tamrin, T., and Wirjosentono, B. (2019). Investigation of TiO_2 doped with nitrogen and vanadium using hydrothermal/Sol-Gel method and its application for dyes photodegradation. *Arab Journal of Basic and Applied Sciences*, *26***(1)**, 242–253.

Marini, A., Hogan, C., Grüning, M., and Varsano, D. (2009). yambo: An ab initio tool for excited state calculations. *Computer Physics Communications*, *180***(8),** 1392–1403.

Matsumoto, Y., Katayama, M., Abe, T., Ohsawa, T., Ohkubo, I., Kumigashira, H., Oshima, M., and Koinuma, H. (2010). Chemical trend of Fermi-level shift in transition metal-doped TiO_2 films. *Journal of the Ceramic Society of Japan*, *118***(1383)**, 993–996.

Mo, L.-B., Wang, Y., Bai, Y., Xiang, Q.-Y., Li, Q., Yao, W.-Q., Wang, J.-O., Ibrahim, K., Wang, H.-H., and Wan, C.-H. (2015). Hydrogen impurity defects in rutile TiO_2. *Scientific Reports*, *5***(1)**, 1–7.

Monkhorst, H. J., and Pack, J. D. (1976). Special points for Brillouin-zone integrations. *Physical Review B*, *13***(12)**, 5188-5191.

Morikawa, T., Asahi, R., Ohwaki, T., Aoki, K., and Taga, Y. (2001). Band-gap narrowing of titanium dioxide by nitrogen doping. *Japanese Journal of Applied Physics*, *40***(6A)**, 561-564.

Mulmi, D. D., Sekiya, T., Kamiya, N., Kurita, S., Murakami, Y., and Kodaira, T. (2004). Optical and electric properties of Nb-doped anatase TiO_2 single crystal. *Journal of Physics and Chemistry of Solids*, *65***(6),** 1181–1185.

Niu, L. (2016). *Bayesian cluster expansion with lattice parameter dependence for studying surface alloys* [PhD Thesis]. Johns Hopkins University.

Paier, J., Marsman, M., Hummer, K., Kresse, G., Gerber, I. C., and Ángyán, J. G. (2006). Screened hybrid density functionals applied to solids. *The Journal of Chemical Physics*, *124***(15)**, 154709-154711.

Parr, R. G. (1980). Density functional theory of atoms and molecules. In *Horizons of quantum chemistry 12***(5)**, 5-15.

Pokluda, J., Černỳ, M., Šob, M., and Umeno, Y. (2015). Ab initio calculations of mechanical properties: Methods and applications. *Progress in Materials Science*, *73*, 127–158.

Ravishankar, T. N., Nagaraju, G., and Dupont, J. (2016). Photocatalytic activity of Li-doped TiO_2 nanoparticles: Synthesis via ionic liquid-assisted hydrothermal route. *Materials Research Bulletin*, *78***,** 103–111.

Richter, J. H., Henningsson, A., Karlsson, P. G., Andersson, M. P., Uvdal, P., Siegbahn, H., and Sandell, A. (2005). Electronic structure of lithium-doped anatase TiO_2 prepared in ultrahigh vacuum. *Physical Review B*, *71***(23)**, 235418-235420.

Roca, R. A., Guerrero, F., Eiras, J. A., and Guerra, J. D. S. (2015). Structural and electrical properties of Li-doped TiO_2 rutile ceramics. *Ceramics International*, *41***(5)**, 6281–6285.

Samat, M. H., Ali, A. M. M., Taib, M. F. M., Hassan, O. H., and Yahya, M. Z. A. (2019). Structural and electronic properties of TiO_2 polymorphs with effective on-site coulomb repulsion term: DFT+ U approaches. *Materials Today: Proceedings*, *17,* 472–483.

Schrödinger, E. (1926). Der stetige Übergang von der Mikro-zur Makromechanik. *Naturwissenschaften*, *14*(**28**), 664–666.

Sedghi-Ghamchi, H., Hassanzadeh, A., Talebian, M., and Mahmoodi-Chenari, H. (2007). Thickness influence on optical and electrochemical properties of dititanium trioxide (Ti_2O_3) films deposited on glass substrates by electron beam gun evaporation. *Physica B: Condensed Matter*, *389*(**2**)*,* 329–334.

Shan, N., Zhou, M., Hanchett, M. K., Chen, J., and Liu, B. (2017). Practical principles of density functional theory for catalytic reaction simulations on metal surfaces – from theory to applications. *Molecular Simulation*, *43*(**10–11**), 861–885.

Sholl, D., and Steckel, J. A. (2011). *Density functional theory: A practical introduction*. John Wiley and Sons.

Shon, H. K., Vigneswaran, S., Kim, I. S., Cho, J., Kim, G. J., Kim, J. B., and Kim, J.-H. (2007). Preparation of Titanium Dioxide (TiO_2) from Sludge Produced by Titanium Tetrachloride ($TiCl_4$) Flocculation of Wastewater. *Environmental Science* and *Technology*, *41*(**4**), 1372–1377.

Slater, J. C., and Krutter, H. M. (1935). The Thomas-Fermi method for metals. *Physical Review*, *47*(**7**), 559-562.

Togo, A., and Tanaka, I. (2015). First principles phonon calculations in materials science. *Scripta Materialia*, *108,* 1–5.

Turner, P. J. (2005). XMGRACE, Version 5.1. 19. *Center for Coastal and Land-Margin Research, Oregon Graduate Institute of Science and Technology, Beaverton, 3* (**4**)*,* 16–18.

Vanderbilt, D. (1990). Soft self-consistent pseudopotentials in a generalized eigenvalue formalism. *Physical Review B*, *41*(**11**), 7892-7898.

Wu, M.C., Lin, T.-H., Chih, J.-S., Hsiao, K.-C., and Wu, P.-Y. (2017). Niobium doping induced morphological changes and enhanced photocatalytic performance of anatase TiO_2. *Japanese Journal of Applied Physics*, *56***(4S)**, 04CP07-04CP11.

Yang, G., Jiang, Z., Shi, H., Xiao, T., and Yan, Z. (2010). Preparation of highly visible-light active N-doped TiO_2 photocatalyst. *Journal of Materials Chemistry*, *20***(25),** 5301–5309.

APPENDIX

APPENDIX A: Structural optimization

A1: Structural optimization

Relaxing atoms in the x, y, and z directions until the systems had the lowest energy positions was used to optimize structural parameters. The following were the outcomes.
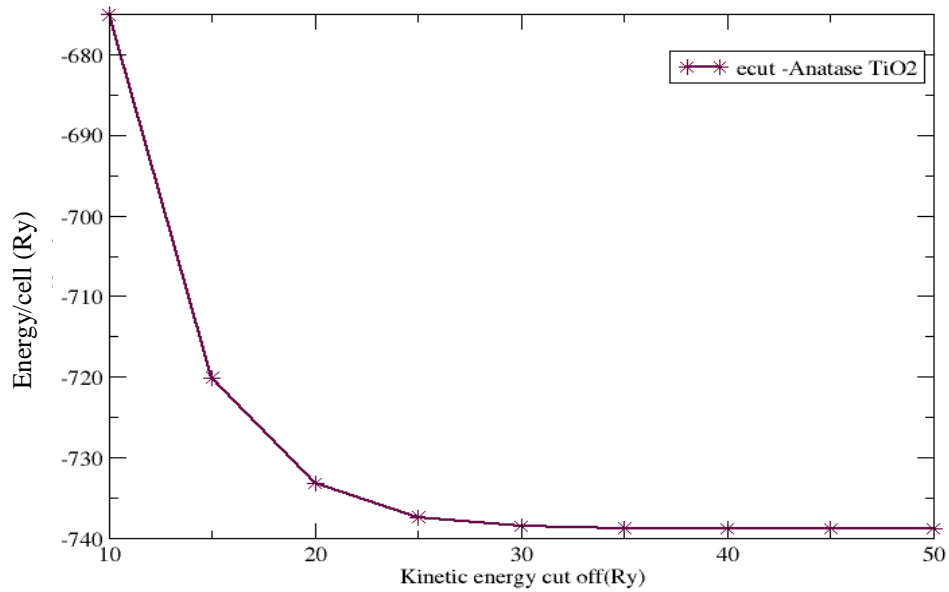
Figure 6.1: Energy/cell versus kinetic energy cut off of the TiO_2 anatase phase.
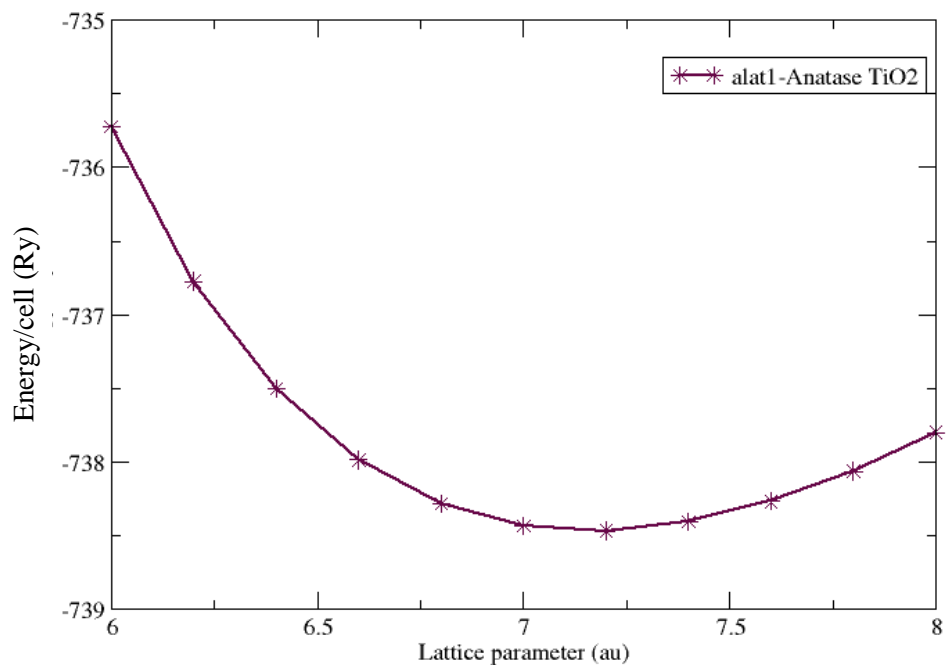
Figure 6.2: Energy/cell versus lattice parameter 'a' of TiO_2 anatase phase
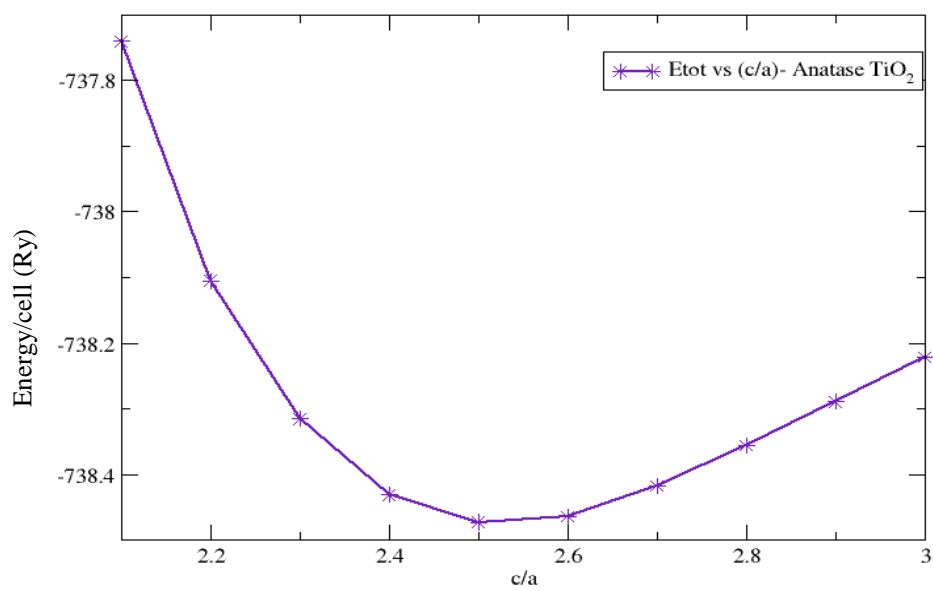
Figure 6.3: Energy/cell versus cell parameter c/a of TiO_2 anatase phase
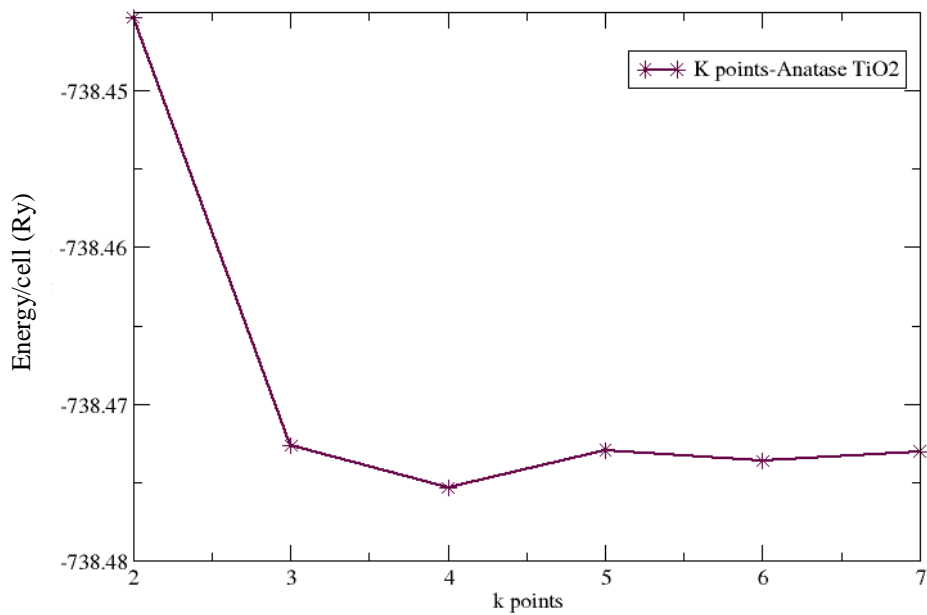
Figure 6.4: Energy/cell versus k- points of TiO$_2$ anatase phase
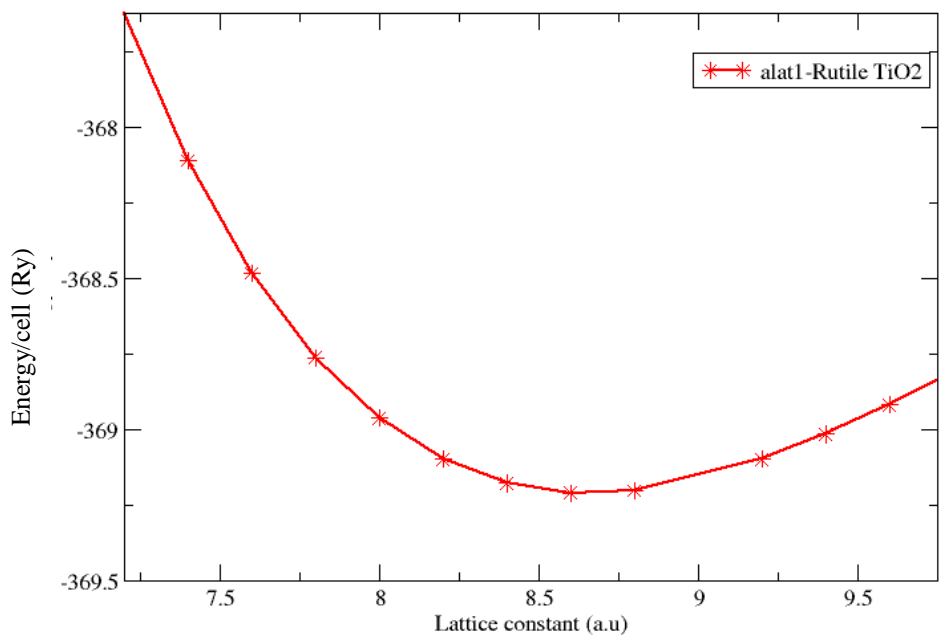
Figure 6.5: Energy/cell versus lattice constant of TiO$_2$ rutile phase
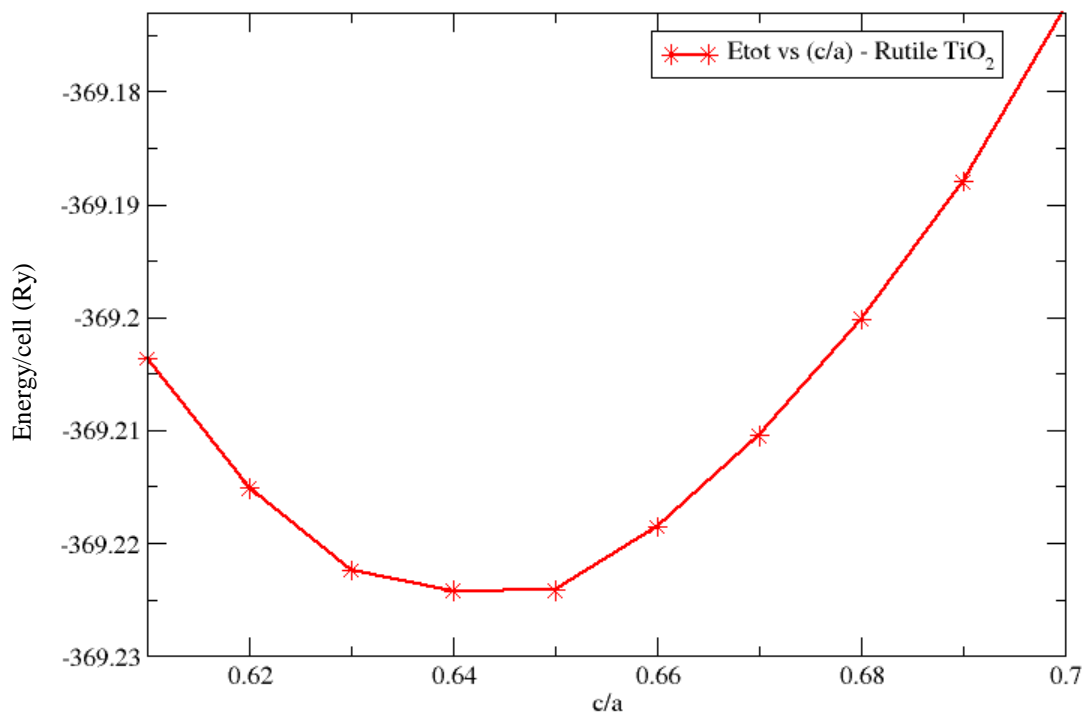
Figure 6.6: Energy/cell versus c/a of TiO$_2$ rutile phase
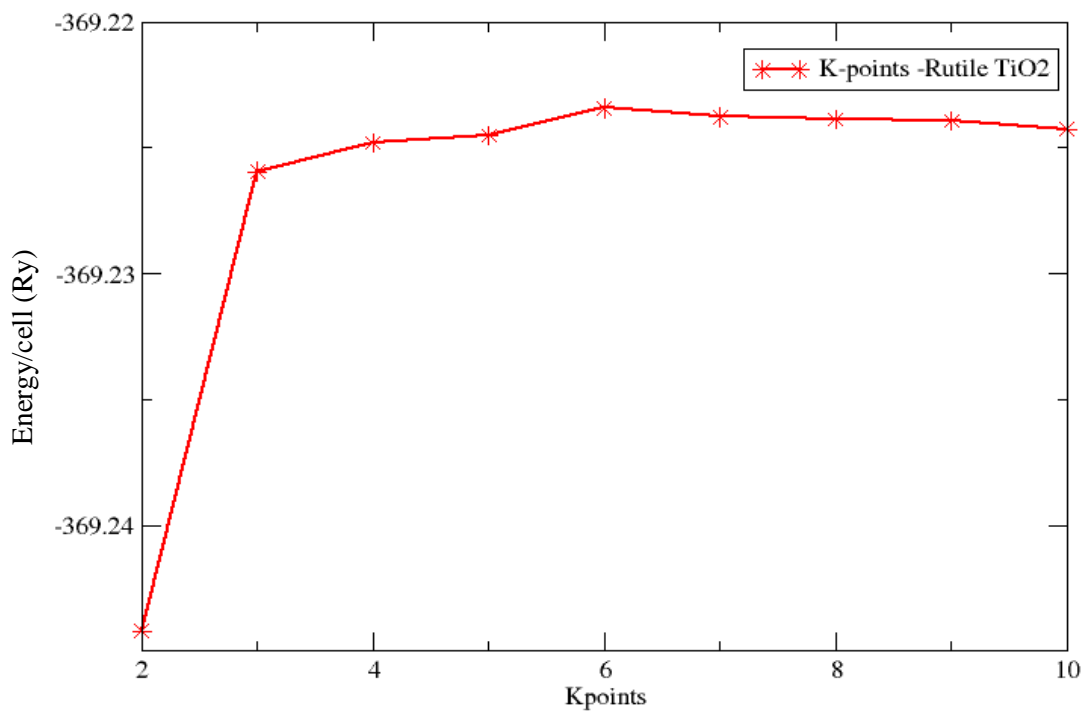
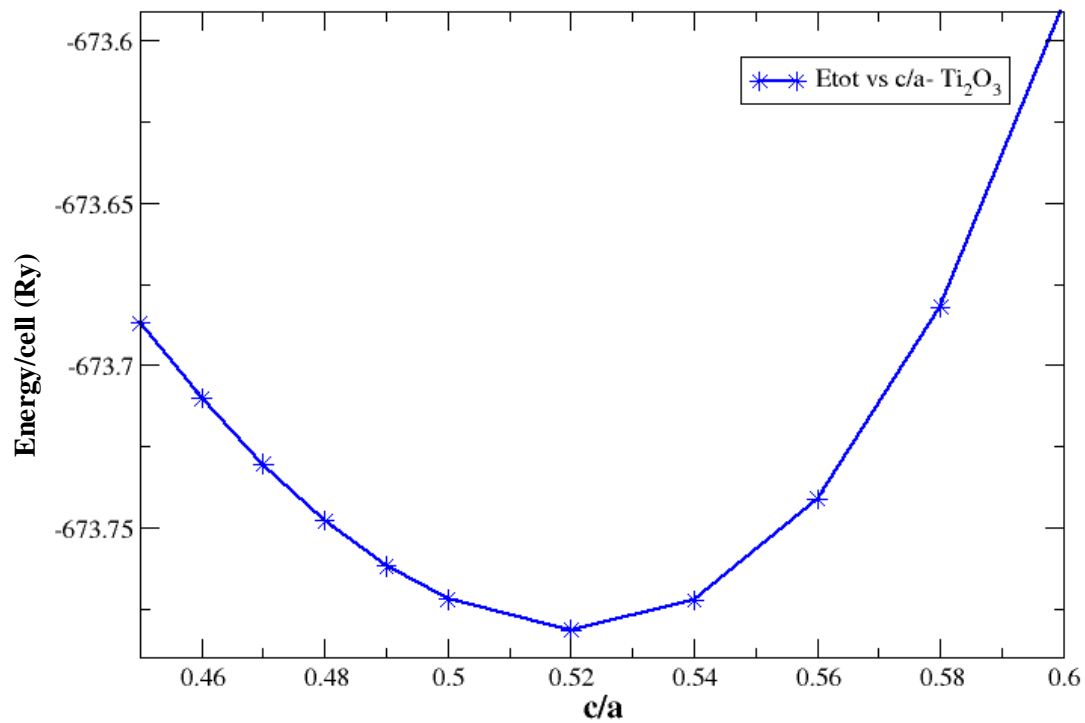**Figure 6.7:** Energy/cell versus k points of TiO$_2$ rutile phase

Figure 6.8: Energy/cell versus cell dimension (c/a) of Ti_2O_3
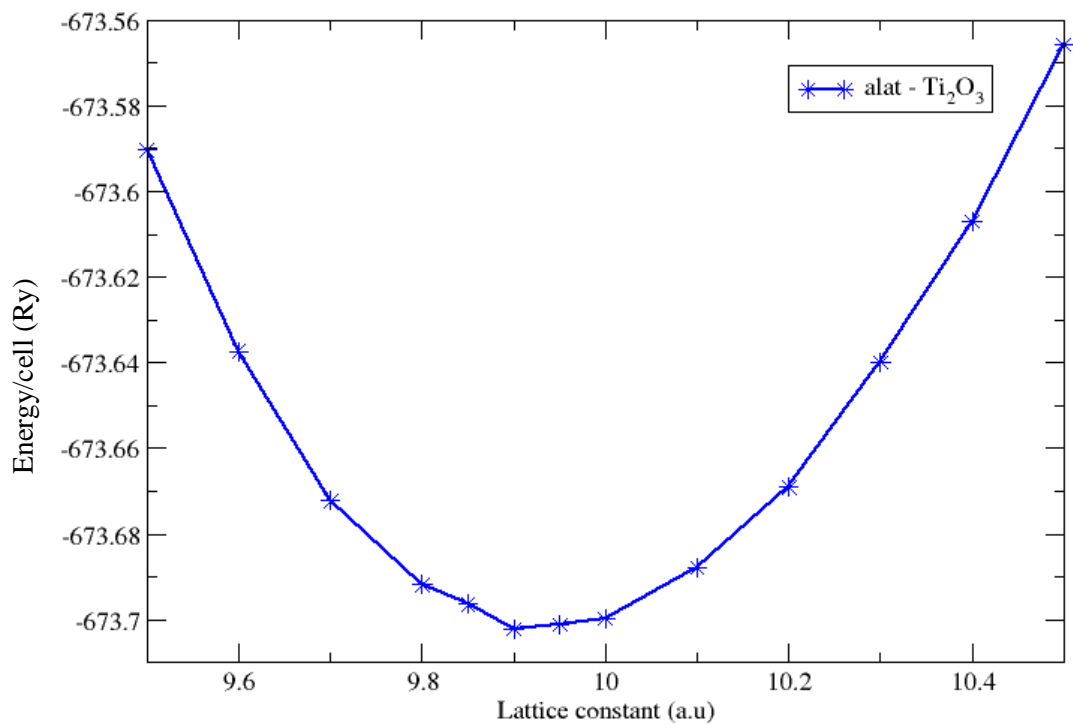
Figure 6.9: Energy/cell versus the lattice parameter of Ti_2O_3

Figure 6.10 shows the values of minimum energies obtained with regard to the relevant k-point grids. Because the structure is well converged at this k-points mesh, a (5x5x5) mesh of Monkhorst-pack special k-points was chosen.
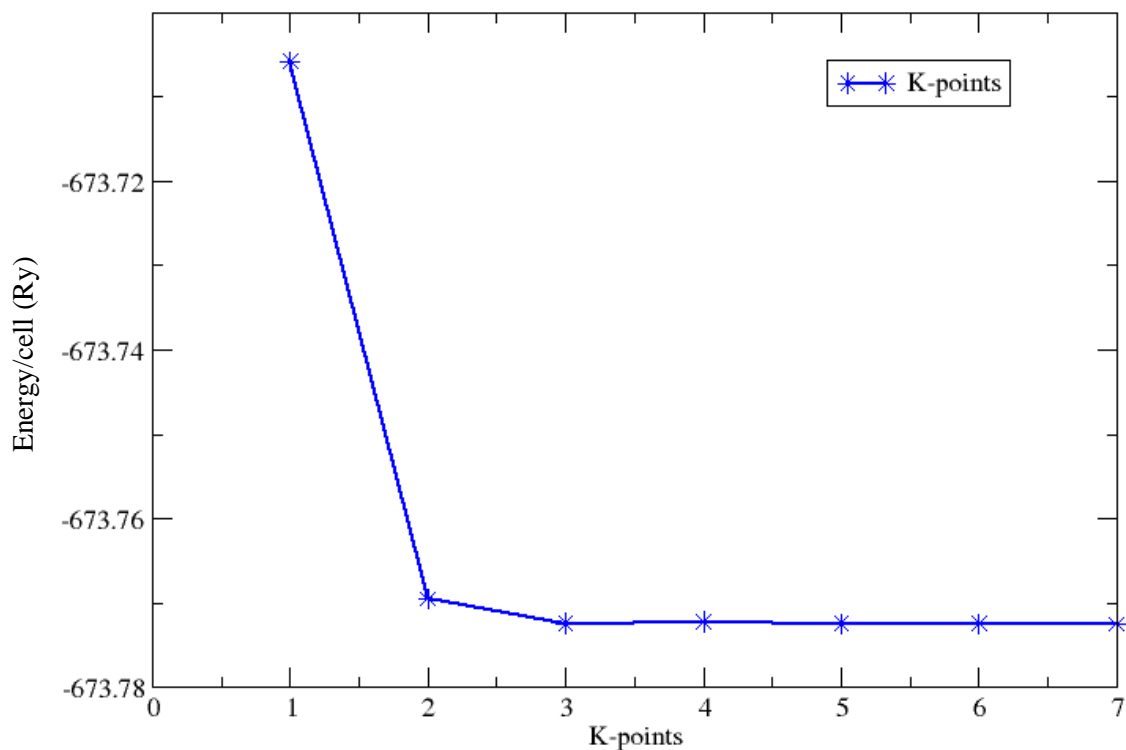

Figure 6.10: A graph of total energy against k-points of Ti_2O_3

The cut-off energy was determined by convergence tests. The plane wave cutoff energies were calculated using a converged k-point grid (ecut). The cutoff energy ranged from 10 Ry to 80 Ry. For Ti_2O_3 structures, 35Ry was chosen as the best cutoff energy.
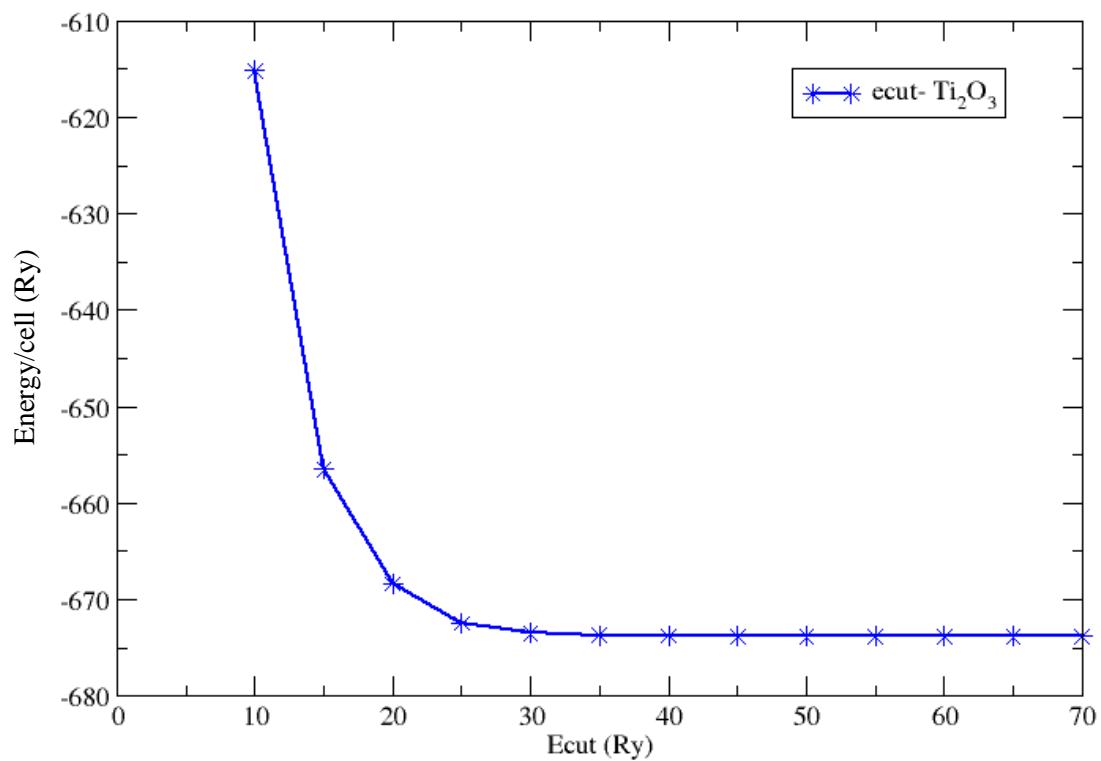
Figure 6.11: Energy/cell versus the cut-off energy of Ti$_2$O$_3$.

APPENDIX B: Pseudopotential files

The pseudopotentials used in these calculations are:

Ti	Ti.pbesol-spn-rrkjus_psl.1.0.0.UPF
O	O.pbesol-nl-rrkjus_psl.1.0.0.UPF
N	N.pbesol-n-rrkjus_psl.1.0.0.UPF

B1: Oxygen pseudopotential file

<UPF version="2.0.1">
 <PP_INFO>
  Generated using "atomic" code by A. Dal Corso v.6.1 svn rev. 13369
  Author: ADC
  Generation date: 9Dec2018
  Pseudopotential type: USPP
  Element: O
  Functional: PBESOL

  Suggested minimum cutoff for wave functions: 43. Ry
  Suggested minimum cutoff for charge density: 316. Ry
  The Pseudo was generated with a Scalar-Relativistic Calculation
  Local Potential by smoothing AE potential with Bessel fncs, cutoff radius: 1.1000
  Pseudopotential contains additional information for GIPAW reconstruction.

  Valence configuration:
  nl pn l occ   Rcut   US   E pseu
  2S 1 0 2.00   1.000   1.300   -1.749893
  2P 2 1 4.00   0.900   1.450   -0.659584
  Generation configuration:
  2S 1 0 2.00   1.000   1.300   -1.749890
  2S 1 0 0.00   1.000   1.300   1.000000

2P 2 1 4.00   0.900   1.450   -0.659581

2P 2 1 0.00   0.900   1.450   0.050000

Pseudization used: troullier-martins

B2: Ti Pseudopotential file

<UPF version="2.0.1">
 <PP_INFO>
  Generated using "atomic" code by A. Dal Corso v.6.1 svn rev. 13369
  Author: ADC
  Generation date: 9Dec2018
  Pseudopotential type: USPP
  Element: Ti
  Functional: PBESOL

  Suggested minimum cutoff for wave functions: 52. Ry
  Suggested minimum cutoff for charge density: 576. Ry
  The Pseudo was generated with a Scalar-Relativistic Calculation
  Local Potential by smoothing AE potential with Bessel fncs, cutoff radius: 1.6000
  Pseudopotential contains additional information for GIPAW reconstruction.

  Valence configuration:
  nl pn l occ   Rcut   Rcut US   E pseu
  3S 1 0 2.00   0.850   1.300   -4.590012
  4S 2 0 2.00   0.850   1.300   -0.329044
  3P 2 1 6.00   0.800   1.600   -2.849877
  3D 3 2 2.00   0.800   1.500   -0.314207
  Generation configuration:
  3S 1 0 2.00   0.850   1.300   -4.590048
  4S 2 0 2.00   0.850   1.300   -0.329052

```
3P  2  1  6.00     0.800     1.600    -2.849907

4P  3  1  0.00     0.800     1.600     4.000000

3D  3  2  2.00     0.800     1.500    -0.314229

3D  3  2  0.00     0.800     1.500     0.050000
```

Pseudization used: troullier-martins

B3: N pseudopotential file

<UPF version="2.0.1">
  <PP_INFO>

Generated using "atomic" code by A. Dal Corso v.6.3MaX

Author: ADC

Generation date: 4Sep2018

Pseudopotential type: USPP

Element: N

Functional: PBESOL

   Suggested minimum cutoff for wave functions: 44. Ry

   Suggested minimum cutoff for charge density: 364. Ry

   The Pseudo was generated with a Scalar-Relativistic Calculation

   Local Potential by smoothing AE potential with Bessel fncs, cutoff radius: 1.2000

   Pseudopotential contains additional information for GIPAW reconstruction.

   Valence configuration:

```
nl pn l  occ     Rcut   Rcut US     E pseu
2S  1  0  2.00    1.000    1.300    -1.356474
2P  2  1  3.00    0.900    1.350    -0.517147
```

   Generation configuration:

```
2S  1  0  2.00     1.000    1.300    -1.356467
2S  1  0  0.00     1.000    1.300     2.000000
2P  2  1  3.00     0.900    1.350    -0.517143
2P  2  1  0.00     0.900    1.350     0.050000
```

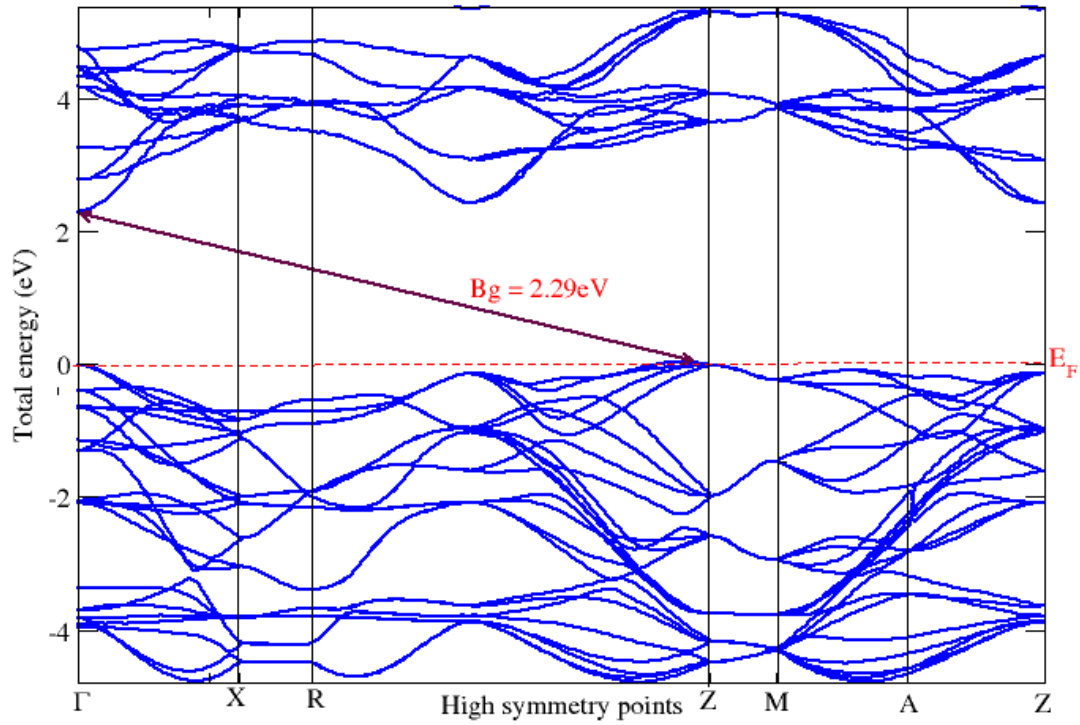   Pseudization used: troullier-martins

APPENDIX C: Band structures
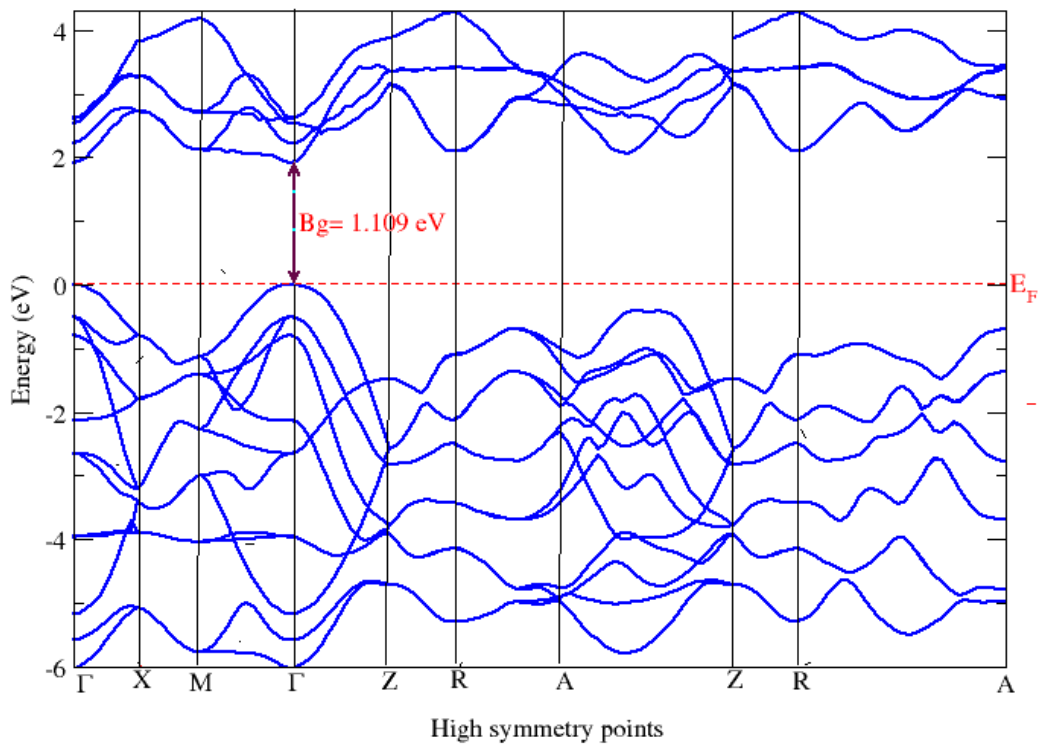

Figure 6.12: Band structure for Bulk Anatase TiO_2.

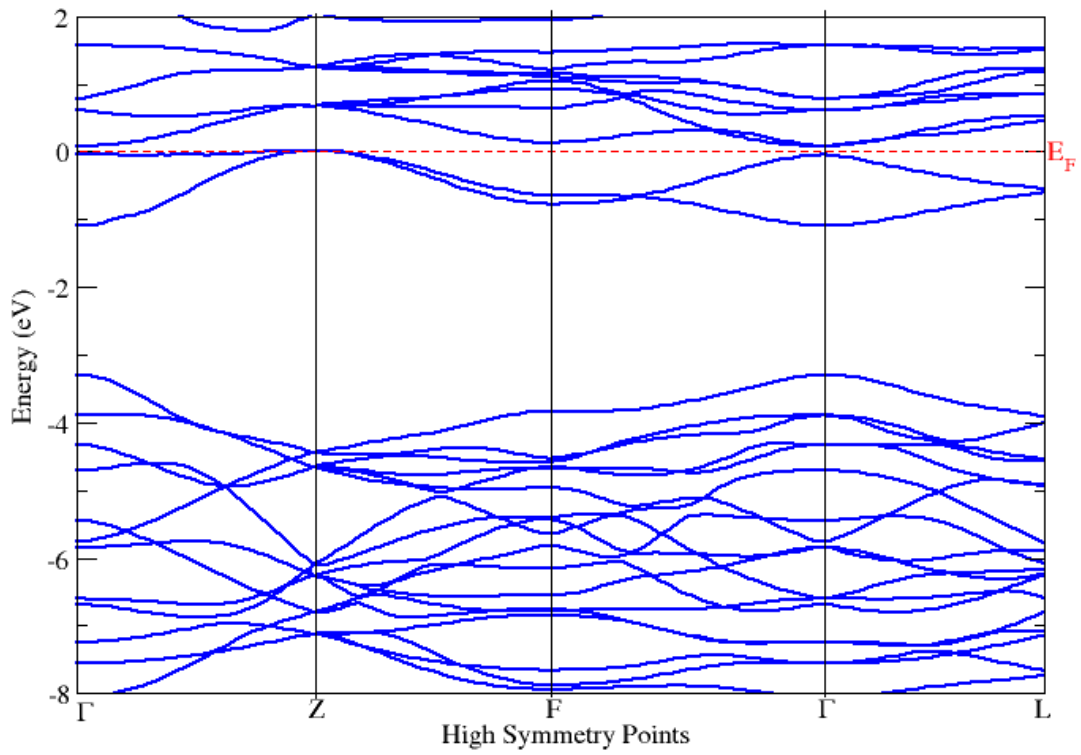**Figure 6.13:** Band structure for Rutile TiO_2

Figure 6.14: Band structure for Corundum Ti$_2$O$_3$.

APPENDIX D: Sample input File

Rutile TiO$_2$ Input File

```
%control
calculation = 'scf'
restart_mode='from_scratch',
prefix='TiO2_Rutile',
pseudo_dir = '/mnt/lustre/users/lallan/PSEUDOPOTENTIALS/',
outdir='./tmp'
verbosity='high'
 /
%system
ibrav= 6, celldm(1)=8.6, celldm(3)= 0.65,
nat= 6, ntyp= 2, ecutwfc = 30.0, ecutrho = 240.0,
occupations='smearing', smearing='gauss', degauss=0.01,
 /
%electrons
mixing_mode = 'plain'
mixing_beta = 0.3
 /
ATOMIC_SPECIES
 Ti 47.900 Ti.pbesol-spn-rrkjus_psl.1.0.0.UPF
 O 15.999  O.pbesol-nl-rrkjus_psl.1.0.0.UPF
ATOMIC_POSITIONS (crystal)
Ti     0.000000000  0.000000000  0.000000000
Ti     0.500000000  0.500000000  0.500000000
O      0.696461465  0.696461465  0.000000000
O      0.303538535  0.303538535  0.000000000
O      0.196472199  0.803527801  0.500000000
O      0.803527801  0.196472199  0.500000000

K_POINTS {automatic}
6 6 4 0 0 0
```